Real-time Magnetic Resonance Imaging

Journal:	*Journal of Magnetic Resonance Imaging*
Manuscript ID	JMRI-20-1018.R1
Wiley - Manuscript type:	Review Article
Classification:	Fast and ultrafast imaging < Imaging Principles and Education < Basic Science, Imaging techniques and processing < Imaging technology and safety < Basic Science, Education < Imaging Principles and Education < Basic Science, Motion supression algorithms < Imaging technology and safety < Basic Science
Manuscript Keywords:	real-time MRI, interactive imaging, rapid imaging

Note: The following files were submitted by the author for peer review, but cannot be converted to PDF. You must view these files (e.g. movies) online.

01_Cardiac_SSFP_TGA_Radial_12x.avi
02_Cardiac_Flow_GA_Spiral.mp4
03_Cardiac_Fetal.avi
04_InterventionalMovie.mp4
05_MRI-RHC.mp4
06_MRI-Thermometry.mp4
07_UpperAirway_Speech_Spiral.mp4
08_UpperAirway_SleepApnea_RadialSMS.mp4
09_UpperAirway_Swallow_RadialFLASH.avi
10_Musculoskeletal_Knee.avi
11_Musculoskeletal_Wrist_Rad_Uln_Dev.mp4
12_Musculoskeletal_TMJ.mp4
13_MLAI_Cardiac_Recon.mp4
14_MLAI_Speech_Deblurring.mp4
15_HPLF.mp4

Real-time Magnetic Resonance Imaging

Journal of Magnetic Resonance Imaging (Review)

ABSTRACT

Real-time magnetic resonance imaging (**RT-MRI**) allows for imaging dynamic processes as they occur, without relying on any repetition or synchronization. This is made possible by modern MRI technology such as fast-switching gradients and parallel imaging. It is compatible with many (but not all) MRI sequences, including spoiled gradient echo, balanced steady-state free precession, and single-shot rapid acquisition with relaxation enhancement. RT-MRI has earned an important role in both diagnostic imaging and image guidance of invasive procedures. Its unique diagnostic value is prominent in areas of the body that undergo substantial and often irregular motion, such as the heart, gastrointestinal system, upper airway vocal tract, and joints. Its value in interventional procedure guidance is prominent for procedures that require multiple forms of soft tissue contrast, as well as flow information. In this review, we discuss the history of RT-MRI, fundamental tradeoffs, enabling technology, established applications, and current trends.

Key Words: Real-Time MRI, Fast Imaging, Interactive Imaging.

INTRODUCTION

Real-time magnetic resonance imaging (**RT-MRI**) enables rapid and continuous acquisition of images that allows visualization of dynamic processes as they occur. RT-MRI does not rely on any gating, synchronization, or repetition of the underlying movement or contrast dynamics. The quality of RT-MRI has experienced major leaps in the past 30+ years due to advances in MRI technology, including fast switching gradients, array receiver coils, and advanced reconstruction including parallel imaging, compressed sensing, and artificial intelligence. Over this same time window, RT-MRI has earned a substantial role in both diagnostic imaging and in the image guidance of invasive procedures. Diagnostic RT-MRI has proven most valuable in areas of the body that undergo substantial and irregular motion, such as the heart (e.g. arrhythmia), upper airway vocal tract (e.g. speech production), joints (e.g. instability), and gastrointestinal system (e.g. motility). RT-MRI for interventional guidance has proven most valuable for procedures that require multiple forms of soft tissue contrast, as well as flow information (e.g. right heart catheterization).

Historically, MRI has had a reputation of being a “slow” modality, especially compared to X-ray, CT, and Ultrasound. This perception is changing. On modern commercial MRI equipment, RT-MRI is now feasible, practical, and readily available. It is compatible with most MRI sequences, and notably includes proton density (**PD**) and T1-weighted (**T1w**) spoiled gradient echo (**GRE**), balanced steady-state free precession (**bSSFP**), and single-shot rapid acquisition with relaxation enhancement (**RARE**). RT-MRI can provide more than adequate spatio-temporal resolution, contrast-to-noise efficiency, and image quality for a wide array of applications.

The purpose of this review is to summarize current state-of-the-art RT-MRI technology and clinical applications, predominantly focussing on imaging of dynamic motion. We begin with a discussion of the history of RT-MRI and fundamental tradeoffs. We then review enabling technology, which includes hardware, acquisition, reconstruction, interaction, and post-processing. Next, we review the most common applications, including cardiac, interventional, upper airway, and musculoskeletal. Finally, we discuss current trends, including the use of machine learning and the use of high-performance low-field MRI systems.

There has been some recent debate regarding nomenclature for RT-MRI (1,2). In this manuscript, *RT-MRI* will refer to real-time acquisition that does not use any gating,

synchronization, or repetition of the movement. We use the term *interactive RT-MRI*, when latency between acquisition and image display is short enough to permit interaction (e.g. guidance of interventions, or calculation of real-time cardiac output).

BRIEF HISTORY

Real-time techniques are commonly used in medical imaging; including live video for gait analysis, fluoroscopy for diagnostic studies of the gastrointestinal tract, and ultrasound to guide interventional procedures such as biopsies. Development toward fast MRI began shortly after the first medical applications. This included the development of Echo Planar Imaging (**EPI**) by Sir Peter Mansfield in 1977 (3), as well as introduction of fast low angle shot magnetic resonance imaging (**FLASH**) by Haase *et al.* in 1986 (4), and fast spin-echo imaging (**RARE**) by Hennig *et al.* in 1986 (5). Early clinical applications of real-time imaging include MR fluoroscopic images of the head by Farzaneh *et al.* in 1989 (6), followed by techniques to interactively control scan slice orientation and image contrast by Holzinger *et al.* in 1990 (7), and real-time flow measurements by Riederer *et al.* in 1991 (8).

More recent developments have enabled substantial progress in MRI acquisition speed, which are discussed below. There has been tremendous growth in the number of publications on RT-MRI, as shown in **Figure 1**. Many of the large vendors have adopted the use of interactive RT-MRI for localization and scan plane/volume prescription. And several diagnostic and interventional applications have developed and matured.

FUNDAMENTAL TRADEOFFS

MRI in general must balance a tradeoff between spatial resolution, temporal resolution, signal-to-noise ratio, artifacts, reconstruction latency, and modeling assumptions. This tradeoff is put to the test in RT-MRI, where temporal resolution is at a premium. **Figure 2** shows a scatter plot of spatial resolution (x-axis) versus temporal resolution (y-axis) from 22 recent publications that utilize state-of-the-art 2D RT-MRI techniques. These publications, with acquisition details listed in **Supplemental Table 1**, were selected to include a diversity of imaging methods and target applications, and to include work from different laboratories both with and without specialized hardware and software capability. The general tradeoff is

illustrated by a gray shaded bar, with fine spatial resolution and coarse temporal resolution on the upper left (e.g. 1x1mm^2 with 80 ms temporal resolution, 12.5 fps), and coarse spatial resolution and fine temporal resolution on the right (e.g. 3.5x3.5mm^2 with 20 ms temporal resolution, 50 fps). Deviations from this line occur because the data span several different applications, reconstruction methods, coil geometries, field strengths, and modelling assumptions. The impact of these is discussed in detail in the Enabling Technology section below. In general, moving towards the lower left requires using more advanced technology, advanced modelling, and increased computational demand, or accepting worse SNR and/or more severe image artifacts.

ENABLING TECHNOLOGY

RT-MRI is made possible by several system components that are included in most modern high-end clinical MRI systems. These beneficial components are discussed in this section. Items that are non-standard are clearly identified.

Hardware

The speed of MRI is fundamentally limited by NMR relaxation, and the time required to cover k-space. RT-MRI therefore relies on time-efficient spatial encoding. One major technological advance has been high-fidelity fast-switching shielded gradients, with eddy-current precompensation. Modern systems offer this with gradients that can produce ≥40mT/m amplitude and ≥150mT/m/ms slew rate on each physical axis with 50-100% duty cycle. This enables GRE and bSSFP contrast with very short repetition times and enables efficient k-space sampling (e.g. spiral or echo-planar). Spiral and EPI trajectories were among the first technical advances to substantially broaden the set of applications that could be addressed with RT-MRI (9).

RT-MRI also benefits from the use of parallel imaging, which requires carefully designed receiver coils arrays that provide diverse coil sensitivity along the likely directions of spatial encoding and k-space undersampling. These coils should preferably preserve body-noise dominance (10). Several MRI manufacturers and third-party vendors manufacture such coils and optimized cardiac and torso coils are readily available. However, coils for nascent

applications such as speech (11,12), and dynamic musculoskeletal imaging are not yet standardized, and there is substantial room for development.

Interactive RT-MRI requires the use of a flexible programmable console that can allow "on-the-fly" changes to the scan plane, shim, and many other imaging parameters. Several modern systems offer this capability, wherein many aspects of a pulse sequence can be modified without substantial interruption (i.e. within a few milliseconds).

Data Acquisition

High frame-rate RT-MRI has been fundamentally enabled by two gradient echo sequences: GRE and bSSFP (**Figure 3A**). RF-spoiled and gradient-spoiled GRE sequences are robust to artifacts and provide T1-weighted contrast with a short repetition time (**TR**). bSSFP sequences (13) provide higher signal-to-noise ratio (**SNR**) efficiency than GRE, and provide T2/T1 contrast, which is extremely advantageous in cardiac imaging because of the excellent blood–myocardium contrast (**Figure 3A**, right). However, bSSFP has two important limitations. One is sensitivity to off-resonance, which manifests as banding artifacts (14). bSSFP RT-MRI is often used at ≤1.5T or at 3T with careful shimming over the region of interest (**ROI**) and with the shortest possible TR. The second issue is a transient approach to steady state, which can be problematic if the application requires frequent switching of the scan plane or volumes, or if there is flow or motion through regions that experience the banding artifact. Transient signal oscillations can be easily mitigated using catalyzation preparation schemes, however it still takes time to reach steady state contrast.

RT-MRI has been made possible by efficient k-space sampling trajectories (e.g. spiral and EPI, described in the preceding section) and clever temporal undersampling schemes. Although it is inefficient, 2DFT imaging may be used in both 2D and 3D imaging due to the simplicity of reconstruction and robustness to artifacts. A wide range of $\vec{k}$-t under-sampling schemes exists for accelerated 2DFT imaging (15–20). For example, one can use variable-density pseudo-random $\vec{k}$-t sampling, which creates incoherent aliasing artifacts in a certain transform domain that can be resolved by advanced reconstruction algorithms.

Figure 3B illustrates more efficient sampling trajectories. EPI (3) is an alternative where multiple Cartesian lines are acquired after each excitation, therefore k-space can be filled only with one or fewer repetitions. However, its long readout time makes it vulnerable

to ghosting and distortions from gradient waveform inaccuracy or off-resonance and near-RT correction methods (21,22) have been proposed.

Most preferred are radial and spiral samplings when higher spatial and/or temporal resolution is desired. Both spiral and radial sampling naturally oversample the center of k-space and this offers motion robustness and tolerance to undersampling. While radial sampling is $\pi/2$ less efficient than Cartesian, its motion robustness and tolerance to undersampling make it popular RT-MRI acquisition method (23). With moderate angular undersampling along with the golden angle scheme (24), the streaking artifacts are usually mild in appearance and incoherent over time. Alternatively, spirals can be very efficient methods to cover k-space. Single-shot spirals can completely cover k-space, but the resultant long readout time increases sensitivity to off-resonance, resulting in spatial blurring. Multi-shot spiral acquisitions with a short readout time can be used to alleviate blurring. Both radial and spiral imaging can be accelerated with the use of $\vec{k}$-t sampling strategies such as under-sampling and random angle order schemes, e.g., bit-reversed (9) or golden angle (24,25) (**Figure 3C**). For instance, radial or spiral imaging can be performed with an angle incremented by the golden angle (222.5°) (24) or tiny golden angles (26). This, when undersampled, produces relatively incoherent aliasing in the spatial and temporal domain (or in a transform domain), which is well-suited for advanced reconstruction algorithms. The view order is an added variable and the golden angle scheme is widely used as it additionally has the retrospective field-of-view (**FOV**) tradeoff ability as opposed to the conventional scheme (right, **Figure 3C**).

RT-MRI has also benefited from 2D multi-slice imaging (11,27–31), which can be performed by utilizing time-interleaved sampling of acquisition schemes described above with a corresponding reduction in spatial or temporal resolution by the number of slices. Alternatively, simultaneous multi-slice imaging (32) can be utilized to accelerate data acquisition. Especially, controlled aliasing in parallel imaging results in higher acceleration, also known as CAIPIRINHA (33,34), has shown substantially reduced aliasing artifacts. This technique has recently been explored in some RT-MRI studies (35–37). 3D imaging has also been explored by extending 2D acquisition schemes to 3D or by using novel 3D sampling trajectories. Radial or spiral can readily be extended to 3D stack-of-stars (38) or 3D stack-of-spirals (39,40) by adding phase encoding steps along k_z direction. Echo-volume imaging (41),

a 3D extension of EPI, can achieve time-efficient 3D imaging and has primarily been investigated for brain functional MRI (42). Combinations of two sampling schemes for 3D imaging has also been explored, including EPI (43) and Cartesian sampling (44), each combined with golden–angle radial sampling. There has also been interesting literature where volumetric image can be efficiently obtained by RT-MRI acquisitions with automatic advancement of the slice position (45). While 3D acquisitions allow for a more flexible $\vec{k}$-t sampling strategy and therefore much redundant information to be exploited along the additional dimension, the increased amount of data is challenging in terms of data processing and reconstruction.

Reconstruction

RT-MRI data sampling and reconstruction varies with application. This is because there is a trade-off between temporal resolution and reconstruction time (governed by the complexity of the algorithm). The simplest reconstruction techniques use data sharing strategies, for example keyhole or sliding window reconstruction (46). This simplicity enables low latency reconstruction; however, the true temporal resolution is coarse.

Higher levels of acceleration are achievable by undersampling, however zero-filled reconstruction results in spatial aliasing that renders the images clinically unusable. One can use parallel imaging to recover usable images, which can be performed in the image domain; SENSitivity Encoding (**SENSE**) (47), or in k-space; GeneRalized Autocalibrating Partial Parallel Acquisition (**GRAPPA**) (48). Parallel imaging of Cartesian data enables very low latency reconstructions; hence its popularity in RT-MRI interventional applications.

Reconstruction of undersampled non-Cartesian data is substantially more complex. This is because the k-space points must be resampled onto a Cartesian grid in order to use the Fast Fourier Transform (**FFT**), which increases computation demand (49). Additionally, in non-Cartesian SENSE each voxel in the image domain can potentially alias with all of the other voxels, resulting in the need for time-consuming iterative reconstructions (50). In non-Cartesian GRAPPA the irregular gaps in k-space, result in the need for geometry-specific GRAPPA weights (51,52) requiring large amounts of calibration data. These drawbacks often restrict the use of non-Cartesian parallel imaging to applications where real-time visualization is not necessary. One exception is through-time GRAPPA where multiple fully sampled non-

Cartesian datasets are acquired and are used to learn the location-specific GRAPPA weights (53–55).

The level of acceleration achievable using parallel imaging, is in theory equal to the number of independent coil elements along the direction of undersampling. In practice, acceleration rates are often limited to 2-3 using Cartesian trajectories, and 3-4 using non-Cartesian trajectories. Higher levels of acceleration can be achieved by combining temporal and spatial encoding schemes. These techniques often leverage the fact that the MR data is sparse in $\vec{x}$-f space, including; $\vec{k}$-t Broad-use Linear Acquisition Speed-up Technique (**BLAST**), $\vec{k}$-t SENSE, $\vec{k}$-t GRAPPA (56). In these schemes, the reconstruction is constrained using some prior information which can be used to determine the ground truth. These techniques often preclude real-time reconstruction as this prior information is extracted from the data itself (57), or as part of a pre-scan.

Even higher acceleration factors are possible using constrained reconstructions (58), compressed sensing (59) and regularized non-linear inversion (**NLINV**) (143). These methods rely on object models, such as sparsity in a known transform domain, along with data sampling that produces incoherent aliasing in the sparsity domain. Some of the most popular sparsifying transforms for RT-MRI are finite differences, total variation, wavelet, and Fourier transform, which can be applied to exploit spatial and/or temporal sparsity. This category of methods enables acquisition of exceptionally high temporal and/or spatial resolution; however, they rely on non-linear reconstruction that is computationally expensive, resulting in high reconstruction latency that often limits clinical adoption.

There has been substantial work towards reducing image reconstruction times. This includes the use of coil selection (60) and coil compression (61) techniques. Modern Graphics Processing Units (**GPU**) enable improvements in latency and throughput, through their massively parallel architecture (62–64), and have enabled up to 27-fold reduction in latency compared to conventional CPUs (65), making interactive RT-MRI feasible.

In addition, the efficient k-space trajectories often used in RT-MRI are susceptible to artifacts from linear time invariant gradient distortions, including eddy currents. Correction of these has been shown to be feasible in real-time (22). However, artifacts from concomitant fields (66,67) are more challenging. At present, these require the use of approximations (68),

or the use of NMR field probes (69,70) in conjunction with a more sophisticated offline reconstruction (71).

Vendor-agnostic raw data formats have been developed to promote reconstruction algorithm sharing and data sharing, for example ISMRM Raw Data (**ISMRMRD**) (72) and Raw Array (**RA**) (73). The ISMRMRD format is designed to support simultaneous streaming of raw data, pulse sequence waveforms, and physiology waveforms, to image reconstruction or processing software (74). This streaming capability is important for fast reconstruction of real time images.

Post-Processing

Offline processing, including segmentation, parameter quantification, and distortion correction, of RT-MRI images is quite similar to traditional offline processing of CINE imaging or even static imaging. However, there are many scenarios where in-line post-processing adds value, particularly for interactive RT-MRI. The unique features of these methods in RT-MRI are that they typically have to tolerate lower image SNR and have to satisfy maximum latency requirements. Inline segmentation has been shown to aid monitoring of ventricular function during cardiac interventions (75). Inline flow quantification has been shown to expedite comprehensive cardiac examinations (76). And, inline off-resonance artifact correction (deblurring) has been shown to substantially improves the sharpness of speech articulator depiction (77).

Interaction/Visualization

RT-MRI applications often benefit from the synchronization with other complementary real-time inputs. For cardiopulmonary testing, physiological monitoring of ECG, respiration, expiratory gases may be synchronized with real-time cardiovascular imaging (75). MRI-guided catheterization requires electrophysiological recording of high-fidelity ECG waveforms, which can be challenging within the MRI environment, and hemodynamic recording of invasive pressure waveforms (78,79). Real-time speech imaging requires synchronization of audio signals with imaging data, which can be achieved with commercial products (e.g. FORMI II+, Optoacoustics Ltd, Israel) (23,80).

Additionally, for some applications, user interaction is required to modify parameters during imaging using real-time feedback to the scanner. Most notably, for real-time MRI guided intervention, the modification of slice position, slice thickness, slice orientation, image contrast, frame rate, and device imaging modules can each be toggled and modified interactively without a pause in the continuous stream of real-time imaging. Interactivity requires that images are displayed and manipulated in real-time, and that pulse sequence parameters are accessible to be modified on-the-fly.

Major MRI vendors have prototype or product graphical user interfaces for interactive imaging (e.g. Monte Carlo prototype, Siemens Healthcare, Erlangen Germany; iSuite, Philips, Best, The Netherlands; iDrive and MR Echo, GE Healthcare, Waukesha, Wisconsin, USA). Interactive imaging platforms are also available through independent MRI software vendors, most notably the RTHawk platform (Heart Vista Inc., Los Altos, CA, USA) (81). This platform is MRI vendor agnostic as long as a fully flexible stub sequence is available, but to-date, has been primarily developed on the GE platform. This system is compatible with interactive scan plane modification using a six degree of freedom 3D mouse (81).

Auxiliary equipment can also be used inside of the MRI suite for interactive modification of imaging. MRI-guided catheterization procedures use foot-pedals to leave interventionist hands available for device manipulation, which mimics traditional X-Ray catheterization suites. Other auxiliary equipment including computer mice, keyboards and tablets have been explored for interactive imaging (82), as well as gesture-based scan control (83). Furthermore, augmented reality and virtual reality equipment (84) may be attractive for interactive visualization of real-time imaging in the future.

APPLICATIONS

RT-MRI benefits a broad range of diagnostic and interventional applications. Here, we summarize the application-specific needs, imaging considerations, and the impact to date.

Cardiac

RT-MRI enables imaging of the cardiovascular system without the need for cardiac gating or respiratory compensation. This is particularly valuable in patients with cardiac

arrhythmia (85,86) where cardiac gating fails (~10% of patients referred for diagnostic cardiac imaging), and in patients who find breath-holding difficult (~10% of patients). It is also extremely valuable in children with congenital heart disease (**CHD**), where it can be used to lessen the need for sedation (87) and its associated risks.

Real-time assessment of cardiovascular structures requires relatively high spatial and temporal resolution to ensure accurate visualization and quantification. For example, Setser et al. (88) recommend a minimum temporal resolution of 50 ms (20 fps), and spatial resolution of 2 mm for functional RT-MRI of the left ventricle. Real-time ventricular function imaging has been shown to achieve an excellent agreement with reference standard breath-held, cardiac gated techniques, through combination of undersampled radial trajectories with $\vec{k}$-t SENSE reconstructions in CHD (89), $\vec{k}$-t SPARSE-SENSE in patients with tachycardia (20) and myocardial infarction (90), regularized non-linear inversion (91) and more recently, proof-of-concept studies using machine learning reconstructions in CHD (92). **Figure 4a** and **Supplemental Movie 1** contains a representative example of image quality. Spiral trajectories, although less popular, have been combined with compressed sensing to achieve high resolution imaging in children with CHD (93).

Quantification of blood flow using phase contrast (**PC**) requires high spatial resolution to mitigate partial volume effects; Greil et al. recommend that it is necessary to have 16 pixels in the cross section of the vessel of interest to get accurate flow quantification (94). PC RT-MRI has been used clinically to assess the respiratory and cardiac components of flow in patients with Fontan circulation (95,96), to quantify flow in children with cardiac left-to-right shunts (97), to investigate the effect of elevated intrathoracic pressure on blood flow (98), and in CHD (99). **Figure 4b** and **Supplemental Movie 2** contains a representative example of image quality.

RT-MRI also enables imaging during exercise, which can be used to unmask subtle changes in early cardiovascular disease (100). Studies have shown the ability to measure ventricular volumes during exercise; to assess the effect of percutaneous pulmonary valve implantation (101), to assess the mechanisms which augment cardiac output with exercise in repaired tetralogy of Fallot (102), and to unmask right ventricular dysfunction in pulmonary arterial hypertension (103). Real-time flow during exercise has also been used in patients with Total Cavopulmonary Connection (104) and after surgical bypass of aortic arch obstruction

(105). Continuous acquisition of real-time flow during ramped exercise over 10 minutes has been shown (62), as well as combination with respiratory gas analysis to simultaneously measure peak oxygen consumption (VO_2) enabling assessment of exercise capacity (106).

Fetal cardiac RT-MRI is of interest as a potential secondary tool (after fetal echocardiography) to characterize congenital cardiac malformations (107). It is one of the most challenging applications of RT-MRI because of the very high heart rates, need for high spatial resolution (tiny hearts), need for interaction (to follow movement of the fetus), and desire to be conservative with SAR and acoustic noise (108). It has been attempted with some success (109), however RT-MRI acquisition with retrospective metric-optimized-gating has provided a promising approach for CINE MRI. **Figure 4c** and **Supplemental Movie 3** contains a representative example of image quality of RT-MRI in the fetal heart.

MRI-guided invasive procedures

MRI-guidance of diagnostic and therapeutic invasive procedures employs intraprocedural imaging to navigate devices and to assess procedural outcomes. Compared to traditional image-guidance modalities such as X-ray and ultrasound, MRI offers flexible image contrast and three-dimensional imaging capabilities that can improve tissue visualization during a procedure. Real-time MRI is particularly valuable during complex device manoeuvres and previous review articles have described the applications of real-time imaging technologies to guide invasive procedures (110–112). **Figure 5** and **Supplemental Movies 4 and 5** contain illustrative examples.

Many invasive procedures have been performed in patients in the MRI environment, including MRI-guided biopsy (113,114); radiotherapy (115); thermal ablations such as radiofrequency ablation (116,117), laser ablation, cryoablation (118), microwave ablation and high intensity focused ultrasound (119); chemoablation; drug injection; electrophysiology (120–122); and invasive pressure measurements (79,123,124).

MRI-guided invasive procedures have unique requirements. Low-latency reconstruction and in-room image display are essential, such that images can be used for real-time device navigation and procedural decision making. Interactivity of imaging parameters is critical to control image contrast and frame rate throughout the procedure. Image processing, including image segmentation, registration and distortion correction, must also

be performed on-the-fly (111). During many invasive procedures, devices (e.g. needles, catheters, guidewires, sheaths) are imaged concurrently with target anatomy. Device imaging is performed using either "passive" visualization, exploiting material properties, or "active" visualization in which devices themselves are RF receivers, designed as loopless antennas for imaging (125) or microcoils for 3D device tracking (126) (**Figure 5A**, **Supplemental Movie 4**). Solenoid and loopless receiver coils positioned on invasive devices can also be applied for small-FOV local imaging in MRI-endoscopy applications (127).

Most in-bore biopsy procedures of prostate, liver, breast, and brain lesions use standard T2-weighted, T1-weighted, diffusion-weighted, or dynamic contrast-enhanced imaging for iterative confirmation of needle placement (113,114,128), with a few studies employing high frame-rate dynamic needle guidance (129,130). MRI-guided cardiovascular procedures are the most technically demanding, requiring rapid multi-planar imaging for device navigation. Most commonly, a 2D Cartesian bSSFP acquisition is used, in combination with parallel imaging, to achieve 5-10 frames/s, with magnetization preparation pulses for contrast variation (**Figure 5B**, **Supplemental Movie 5**). 2D radial and spiral spoiled gradient echo acquisitions have also been applied for cardiovascular procedures (131,132), and when combined with regularized nonlinear inversion reconstruction, have achieved temporal resolution of 42 ms (24 fps) with reconstruction delay of 27 ms (133).

RT-MRI thermometry, using proton resonance frequency shift imaging, is important to monitor thermal ablations with high temporal resolution. Multi-slice single-shot EPI acquisitions with real-time image registration methods have been developed for thermometry and dosimetry during cardiac RF ablations (134,135) (**Figure 5C**, **Supplemental Movie 6**). The geometry of transcranial high intensity focused ultrasound (**HIFU**) therapy devices restricts the number of receive coils that can be positioned around the head, and undersampled stack-of-spiral and stack-of-stars EPI thermometry acquisitions (40,43) have been developed for volumetric brain coverage with 75 ms temporal resolution (13 fps). 3D dynamic keyhole imaging has generated high spatiotemporal resolution (1.5x1.5x6 mm^3 with 455 ms temporal resolution, 2 fps) imaging for dynamic guidance of radiotherapy (136). This work utilizes a super-resolution generative model for high-spatial reconstruction from low-spatial and high-temporal resolution images.

The unique set of requirements of MRI-guided invasive procedures continues to motivate the innovation of RT-MRI acquisitions, as well as rapid inline image reconstruction and image processing.

Upper Airway

RT-MRI enables imaging soft-tissue structures and muscles of the upper airway that are coordinated in space and time to perform essential human functions such as speech, respiration, and digestion. RT-MRI is preferred over other imaging and movement tracking modalities because it allows for observing deep soft-tissues such as the velum, pharyngeal wall, and the larynx in the arbitrary imaging plane without radiation or endoscopy. The nature of the movements of the upper airway is not necessarily periodic and is unrepeatable. RT-MRI can now be combined with intermittent tagging pulses to visualize internal deformation in the tongue muscles (137,138) and be exploited to reconstruct 3D tongue shape or model (139,140). Real-time visualization and interaction are also advantageous for the operator to modify imaging parameters on-the-fly and to ensure subject's compliance with stimuli.

Figure 6 and **Supplemental Movies 7-9** illustrate representative research areas in speech production (23,141), sleep apnea (36,37,142) and swallowing (143). Imaging is often performed along with synchronized recordings of physiological signals such as audio signals in speech (144), polysomnography signals used in sleep studies (36), and intraoral pressure sensor used in swallowing (145) to aid real-time or retrospective analysis. Several clinical applications have also been explored such as velopharyngeal insufficiency (146), apraxia (143,147), and post-surgical assessment of glossectomy (147,148) and cleft-palate repair (149,150). Many other applications and technical aspects of the upper airway imaging have been described in review articles with focuses on speech (23,141,151), speech and sleep (152), sleep (142), and image analysis techniques on RT-MRI of vocal tract motion (153).

The upper airway imaging generally requires high spatial and temporal resolution although specific imaging parameters would be dictated by the applications as shown in Figure 1 in Lingala et al.(23). For speech, high temporal resolution, below 70 ms (greater than 14 fps) and spatial resolution of no more than 3.5 mm^2 are typically required to study a broad range of speech events. For sleep, pharyngeal airway motion is relatively slower than vocal tract motion as it involves closure of the airway, requiring lower temporal resolution than

imaging for speech and swallowing. For swallowing, it is valuable to track both the pharyngolaryngeal area and the lower esophageal sphincter and its surrounding area (154).

Current state-of-the-art technique uses non-Cartesian sampling (radial or spiral acquisition) and parallel imaging, combined with constrained reconstruction. This has enabled 2D dynamic images with spatial resolutions of 1.3 to 2.4 mm^2 at high temporal resolutions of 10 to 60 ms (100 to 17 fps) from highly under-sampled MRI data (11,54,55,145,155–158). Imaging 2D mid-sagittal plane is the most widely used as it is most informative thanks to its entire vocal tract coverage from the lips to the glottis given a high temporal resolution. Imaging a few 2D planes (11,29,30), simultaneous 2D planes (36,37), or 3D (38) at the cost of temporal resolution have also been developed. Recently, 3D stack-of-spiral acquisition demonstrated imaging of the full vocal tract (FOV: 200x200x70 mm^3) with high spatio-temporal resolution (2.4x2.4x5.8 mm^3, with 72 ms temporal resolution, 14 fps) during natural speech (39).

Imaging the upper airway has a unique challenge – tissue surfaces along the upper airway are the main region of interest but are vulnerable to off-resonance effects. Those include the movements of the articulators during speech or swallowing, the closure of the velopharyngeal port in velopharyngeal insufficiency, and the collapse of the pharyngeal airway in sleep study. Off-resonance at the tissue surfaces manifests as blurring or signal loss with non-Cartesian sampling such as spirals and/or appear as banding artifact when bSSFP sequences are used. Careful shimming is usually carried out with a focus on the tissue boundaries. Current RT-MRI studies for speech production are most often conducted using short-duration spirals (2.5 ms) and/or at lower field strength (1.5T or lower) MRI scanners, or in conjunction with field inhomogeneity reconstruction (159–161) or more recently AI-based deblurring (77).

Musculoskeletal

Musculoskeletal RT-MRI is used to reveal abnormal joint biomechanics which are linked to joint disorders, usually in the context of pain, instability or movement restriction. For example, abnormal knee kinematics is known to contribute to the development and progression of osteoarthritis. Common musculoskeletal applications include the knee, wrist, spine, temporomandibular joint, foot, and hip (162), with a selected few illustrated in **Figure**

7 and **Supplemental Movies 10-12**. These have vastly different spatio-temporal resolution and coverage needs.

Early work used semi-static approaches (multiple static images in fixed postures). Systematic studies have since determined that biomechanical models derived from RT-MRI are substantially different from those derived from semi-static approaches (163), making RT-MRI the current method of choice. Musculoskeletal movements are voluntary, and can sometimes be performed through controlled dynamics, for example where movements are repeated and synchronized with a metronome or periodic visual stimulus. However, voluntary synchronization is imprecise, subject-dependent, and impractical for patients with pain. Retrospective gating can be applied using additional sensors (164) or self-gating approaches (165), assuming that the timing variations have a negligible impact on kinematic estimates. Movement can be more precisely controlled by a physical apparatus, but this does not lead to realistic physical effort, which is often needed to reproduce the abnormal movement and/or the symptom being studied (e.g. pain). Finally, it is possible to synchronize using external muscle stimulation (166), which adds experimental complexity. For all of these reasons, there is a need for RT-MRI, and often a need for an appropriate load (167).

Musculoskeletal RT-MRI requires strong contrast between muscle, fat, and surrounding fluids, and benefits from high SNR efficiency, making bSSFP the sequence of choice (168). bSSFP can be augmented with phase-sensitive reconstruction for fat-water separation (169). GRE may also be used with optional multi-echo fat-water separation (170). Most studies in the literature were performed at conventional field strengths (1.5T and 3T) in the supine position, which restricts movement and load bearing. For this reason, low-field open-bore and upright MRI has been explored as an alternative to alleviate these restrictions (171).

In the knee, RT-MRI has provided valuable insight into patellofemoral pain, and used to quantify kinematics (172), document the differences between the load-bearing and non-load-bearing kinematics (173), and determine the effects of physical supports (172). RT-MRI measurement of tibiofemoral kinematics can be further improved by using slice-to-volume registration with 3D static scans (174,175). In the finger, 2D RT-MRI has provided insight into joint cavitation, which is responsible for the cracking sound (176). In the wrist, 2D and 3D RT-MRI have provided insight into ligament insufficiency, instability, and how aberrant

kinematics may contribute to wrist pain (177,178). In the shoulder, low-resolution RT-MRI in conjunction with high-resolution static MRI was used to better characterize rotator cuff disease (179). In the temporomandibular joint, RT-MRI has been demonstrated with adequate spatio-temporal resolution to track disc and condyle kinematics (180,181). In summary, RT-MRI is a promising early-stage technique for studying musculoskeletal kinematic insufficiency/abnormality and pain in several body regions.

Other

RT-MRI has also been used for other thorax and abdominal imaging applications. Real-time cine imaging has been used to assess abnormal bowel motility following ingestion of an oral contrast agent (e.g. mannitol). Bowel imaging is typically performed in a coronal orientation and bSSFP imaging has been applied for imaging for 1-3 s temporal resolution per 3D volume (1 to 0.3 fps) (182,183). Dynamic esophageal imaging has been achieved using a radial spoiled gradient echo acquisition with nonlinear inverse image reconstruction for 40 ms temporal resolution (25 fps) following the ingestion of pineapple juice (184). RT-MRI has also been used in urethrography, to assess urinary function during bladder emptying (185), in defecography, to assess the pelvic floor in mechanical and functional rectal disorders (186) and to asses pelvic floor disorder and pelvic organ prolapse (187). These techniques often use turbo spin-echo sequences to achieve T2 weighting, with 1.0-1.5mm spatial resolution, and a temporal resolution of 1-5 seconds (1 to 0.2 fps).

RT-MRI has also proven valuable for screening of fetal central nervous system abnormalities, specifically the structural malformations (188–190). T2-weighted RARE sequences (often with partial echo along the phase encode direction) are used for the beneficial contrast between gray and white matter.

This paper is focused on the use of RT-MRI in imaging physical motion; however it can also be used to image contrast dynamics. Although this is beyond the scope of this article, this includes dynamic contrast enhanced MRI (191), time-resolved angiography (192), as well as functional MRI (42) including Arterial Spin Labelling (ASL) (193) and Encephalography (194).

CURRENT DIRECTIONS

Increasing Role of ML/AI

In recent years, machine learning methods, especially deep learning, have enabled breakthroughs in computer vision and image analysis. The astonishing success of deep learning algorithms has penetrated areas of MR image reconstruction, artifact correction, automatic classification and segmentation, landmark detection, and so on.

Deep learning has huge potential in RT-MRI applications, for example in real-time visualization and/or immediate downstream analysis. There have been several early works on ML with success for RT-MRI applications, as illustrated in **Figure 8** and **Supplemental Movies 13-14**. This figure demonstrates the use of deep learning for various tasks; reconstruction of RT-MRI data (removing artefact from undersampled radial images, **Figure 8a**), improving image quality of RT-MRI (performing off-resonance deblurring, **Figure 8b**), and to enhance clinical impact (performing Needle detection and segmentation, **Figure 8c)**. It has been shown to be popular for low-latency reconstructions of real-time MR data; in 2D cardiac imaging (92,195,196), MR-guided radiotherapy images (197), and 3D functional MRI (198). Additionally, it is popular for rapid post-processing of real-time data; including identification and segmentation of the vocal tract (199–202), as well as segmentation of the left and right ventricles from real-time cardiac MRI (203). Other applications include rapid needle detection and segmentation in MR-guided interventions (204,205), enabling real-time localization of the Fetal brain (206), spiral off-resonance deblurring in speech imaging (77), and combination of reconstruction and post-processing for real-time MR thermometry (207).

Some commercially available software has started using ML in real-time imaging, including HeartVista (208) which uses ML to automate the MRI exam, control the scanner and assist scan planning, and MeVisLab (209) for segmentation and annotation.

High Performance Low Field

Recent publications have suggested substantial opportunities for real-time imaging on high-performance low field (**HPLF**) MRI systems (210). These systems operate with a low static field strength (e.g. 0.35T and 0.55T) and incorporate contemporary high-performance hardware and modern imaging methods. Unlike historic low field MRI systems, these HPLF systems include fast shielded gradients and multi-channel receiver arrays. They are capable of non-Cartesian sampling, parallel imaging, and compressed sensing, and can exploit readily

available computational resources. These systems have produced new capability and exceptional performance for cardiac, abdominal, and pulmonary RT-MRI, illustrated in **Figure 9** and **Supplemental Movie 15**.

The HPLF system configuration provides several advantages for real-time imaging. 1) Many RT-MRI acquisitions are limited by off-resonance (e.g. bSSFP, spiral). Since absolute off-resonance (in Hz) scales linearly with field strength, lower field strength systems relax this constraint. For bSSFP acquisitions, longer TRs can be used without banding artifacts. For spiral sampling, longer readouts can be used without blurring artifacts. 2) T2* is longer, making it possible for efficient data sampling strategies, including spiral and EPI and to be implemented with prolonged duration. This allows increased flexibility in trajectory design. Moreover, artifacts related to susceptibility (e.g. blurring and ghosting) are reduced. 3) T1 is shorter at lower field strength causing more rapid signal recovery between RF pulses. 4) Tissue heating due to RF is reduced at low field, which permits high flip angle excitation and magnetization preparation pulses, with diminishing concerns of patient safety during prolonged real-time imaging. The net result is a favourable system configuration for real-time imaging.

HPLF is especially beneficial for MR-guided interventions, due to the favourable low SAR properties. Reduced device heating will enable the application of commercial conductive devices in the MRI-environment, and reduce the burden of design for new devices, which is substantial at conventional field strengths (≥1.5T) (211). HPLF is also beneficial for real-time speech imaging, where susceptibility gradients at air-tissue interfaces are the primary constraint.

Finally, a HPLF system could be cost effective to manufacture, install and maintain, which may increase accessibility for these real-time imaging applications outside of the conventional Radiology environment (e.g. cardiology and point-of-care settings). Currently, the B0 subsystem comprises roughly 30% of system cost (212). Therefore, a reduction in field strength and potential complexity (i.e. simplified cooling and maintenance) could enable an attractive value system.

CONCLUDING REMARKS

MRI has historically been applied to static imaging of the brain, spine, and joints, due to its relatively slow speed. Leaps in MRI technology and information extraction over the last

two decades have made it possible to image more broadly, including areas of the body that experience substantial motion and even irregular motion, and including the real-time guidance of interventions. RT-MRI has a rich history and an even brighter future. It is a key enabling technology for MRI to penetrate new diagnostic and interventional applications.

ACKNOWLEDGEMENTS

A.C.W. acknowledges the assistance of Siemens Healthcare in the modification of the NHLBI MRI system for operation at 0.55T under an existing cooperative research agreement between NHLBI and Siemens Healthcare. This system was used to generate Figure 9 and Supplemental Movie 15.

REFERENCES

1. Dietz B, Fallone BG, Wachowicz K. Nomenclature for real-time magnetic resonance imaging. Magn Reson Med. 2019;81(3):1483–4.
2. Nayak KS. Response to Letter to the Editor: "Nomenclature for real-time magnetic resonance imaging." Magn Reson Med. 2019;82(2):525–6.
3. Mansfield P. Multi-planar image formation using NMR spin echoes. J Phys C Solid State Phys. 1977;10:L55–8.
4. Frahm J, Haase A, Matthaei D. Rapid NMR imaging of dynamic processes using the FLASH technique. Magn Reson Med. 1986;3(2):321–7.
5. Hennig J, Nauerth A, Friedburg H. RARE imaging: a fast imaging method for clinical MR. Magn Reson Med. 1986;3(6):823–33.
6. Farzaneh F, Riederer SJ, Lee JN, Tasciyan T, Wright RC, Spritzer CE. MR fluoroscopy: initial clinical studies. Radiology. 1989;171(2):545–9.
7. Holsinger AE, Wright RC, Riederer SJ, Farzaneh F, Grimm RC, Maier JK. Real-time interactive magnetic resonance imaging. Magn Reson Med. 1990;14(3):547–53.
8. Riederer SJ, Wright RC, Ehman RL, Rossman PJ, Holsinger-Bampton AE, Hangiandreou NJ, et al. Real-time interactive color flow MR imaging. Radiology. 1991;181(1):33–9.
9. Kerr AB, Pauly JM, Hu BS, Li KC, Hardy CJ, Meyer CH, et al. Real-time interactive MRI on a conventional scanner. Magn Reson Med. 1997;38(3):355–67.
10. Macovski A. Noise in MRI. Magn Reson Med. 1996;36(3):494–7.
11. Lingala SG, Zhu Y, Kim Y-C, Toutios A, Narayanan S, Nayak KS. A fast and flexible MRI system for the study of dynamic vocal tract shaping. Magn Reson Med. 2017;77(1):112–25.
12. Kim YC, Hayes CE, Narayanan SS, Nayak KS. Novel 16-channel receive coil array for accelerated upper airway MRI at 3 Tesla. Magn Reson Med. 2011;65(6):1711–7.
13. Scheffler K, Lehnhardt S. Principles and applications of balanced SSFP techniques. Eur Radiol. 2003;13(11):2409–18.
14. Reeder SB, Markl M, Yu H, Hellinger JC, Herfkens RJ, Pelc NJ. Cardiac CINE imaging with IDEAL water-fat separation and steady-state free precession. J Magn Reson Imaging. 2005;22(1):44–52.
15. Lustig M, Santos JM, Donoho DL, Pauly JM. k-t SPARSE: high frame rate dynamic MRI

exploiting spatio-temporal sparsity. n: Proceedings of the 14th Annual Meeting of ISMRM, Seattle, Washington, USA, 2006. p. 2420.

16. Feng L, Srichai MB, Lim RP, Harrison A, King W, Adluru G, et al. Highly accelerated real-time cardiac cine MRI using k–t SPARSE-SENSE. Magn Reson Med. 2013;70(1):64–74.
17. Jung H, Sung K, Nayak KS, Kim EY, Ye JC. K-t FOCUSS: a general compressed sensing framework for high resolution dynamic MRI. Magn Reson Med. 2009;61(1):103–16.
18. Otazo R, Kim D, Axel L, Sodickson DK. Combination of compressed sensing and parallel imaging for highly accelerated first-pass cardiac perfusion MRI. Magn Reson Med. 2010;64(3):767–76.
19. Gamper U, Boesiger P, Kozerke S. Compressed sensing in dynamic MRI. Magn Reson Med. 2008;373:365–73.
20. Bassett EC, Kholmovski EG, Wilson BD, DiBella EVR, Dosdall DJ, Ranjan R, et al. Evaluation of highly accelerated real-time cardiac cine MRI in tachycardia. NMR Biomed. 2014;27(2):175–82.
21. Kim Y-C, Nielsen J-F, Nayak KS. Automatic correction of echo-planar imaging (EPI) ghosting artifacts in real-time interactive cardiac MRI using sensitivity encoding. J Magn Reson Imaging. 2008;27(1):239–45.
22. Campbell-Washburn AE, Xue H, Lederman RJ, Faranesh AZ, Hansen MS. Real-time distortion correction of spiral and echo planar images using the gradient system impulse response function. Magn Reson Med. 2016;75(6):2278–85.
23. Lingala SG, Sutton BP, Miquel ME, Nayak KS. Recommendations for real-time speech MRI. J Magn Reson Imaging. 2016;43(1):28–44.
24. Winkelmann S, Schaeffter T, Koehler T, Eggers H, Doessel O. An optimal radial profile order based on the golden ratio for time-resolved MRI. IEEE Trans Med Imaging. 2007;26(1):68–76.
25. Kim YC, Narayanan SS, Nayak KS. Flexible retrospective selection of temporal resolution in real-time speech MRI using a golden-ratio spiral view order. Magn Reson Med. 2011;65(5):1365–71.
26. Wundrak S, Paul J, Ulrici J, Hell E, Rasche V. A small surrogate for the golden angle in time-resolved radial MRI based on generalized Fibonacci sequences. IEEE Trans Med Imaging. 2015;34(6):1262–9.

27. Nayak KS, Pauly JM, Nishimura DG, Hu BS. Rapid ventricular assessment using real-time interactive multislice MRI. Magn Reson Med. 2001;45(3):371–5.

28. Bornstedt A, Nagel E, Schalla S, Schnackenburg B, Klein C, Fleck E. Multi-slice dynamic imaging: complete functional cardiac MR examination within 15 seconds. J Magn Reson Imaging. 2001;14(3):300–5.

29. Kim YC, Proctor MI, Narayanan SS, Nayak KS. Improved imaging of lingual articulation using real-time multislice MRI. J Magn Reson Imaging. 2012;35(4):943–8.

30. Feng X, Inouye JM, Blemker SS, Lin KY, Borowitz KC, Altes T, et al. Assessment of velopharyngeal function with multi-planar high-resolution real-time spiral dynamic MRI. Magn Reson Med. 2018;80:1467–74.

31. Krohn S, Joseph AA, Voit D, Michaelis T, Merboldt K-D, Buergers R, et al. Multi-slice real-time MRI of temporomandibular joint dynamics. Dentomaxillofac Radiol. 2018;48(1):20180162.

32. Larkman DJ, Hajnal J V, Herlihy AH, Coutts GA, Young IR, Ehnholm G. Use of multicoil arrays for separation of signal from multiple slices simultaneously excited. J Magn Reson Imaging. 2001;13(2):313–7.

33. Hamilton JI, Wright KL, Griswold MA, Seiberlich N. Self-Calibrating Interleaved Reconstruction for Through-Time Non-Cartesian GRAPPA. In: Proceedings of the 21st Annual Meeting of ISMRM, Salt Lake City, Utah, USA, 2013. p.3836.

34. Setsompop K, Gagoski BA, Polimeni JR, Witzel T, Wedeen VJ, Wald LL. Blipped-controlled aliasing in parallel imaging for simultaneous multislice echo planar imaging with reduced g-factor penalty. Magn Reson Med. 2012;67(5):1210–24.

35. Rosenzweig S, Holme HCM, Wilke RN, Voit D, Frahm J, Uecker M. Simultaneous multi-slice MRI using cartesian and radial FLASH and regularized nonlinear inversion: SMS-NLINV. Magn Reson Med. 2018;79(4):2057–66.

36. Wu Z, Chen W, Khoo MCK, Davidson Ward SL, Nayak KS. Evaluation of upper airway collapsibility using real-time MRI. J Magn Reson Imaging. 2016;44(1):158–67.

37. Chen W, Gillett E, Khoo MCK, Davidson Ward SL, Nayak KS. Real-time multislice MRI during continuous positive airway pressure reveals upper airway response to pressure change. J Magn Reson Imaging. 2017;46(5):1400–8.

38. Burdumy M, Traser L, Burk F, Richter B, Echternach M, Korvink JG, et al. One-second

MRI of a three-dimensional vocal tract to measure dynamic articulator modifications. J Magn Reson Imaging. 2017;46(1):94–101.

39. Lim Y, Zhu Y, Lingala SG, Byrd D, Narayanan S, Nayak KS. 3D dynamic MRI of the vocal tract during natural speech. Magn Reson Med. 2019;81:1511–1520.
40. Fielden SW, Feng X, Zhao L, Miller GW, Geeslin M, Dallapiazza RF, et al. A spiral-based volumetric acquisition for MR temperature imaging. Magn Reson Med. 2018;79(6):3122–7.
41. Mansfield P, Howseman AM, Ordidge RJ. Volumar imaging using NMR spin echoes: echo-volumar imaging (EVI) at 0.1 T. J Phys E. 1989;22(5):324–30.
42. van der Zwaag W, Francis S, Bowtell R. Improved echo volumar imaging (EVI) for functional MRI. Magn Reson Med. 2006;56(6):1320–7.
43. Jonathan S V, Grissom WA. Volumetric MRI thermometry using a three-dimensional stack-of-stars echo-planar imaging pulse sequence. Magn Reson Med. 2018;79(4):2003–13.
44. Kim Y-C, Lebel RM, Wu Z, Ward SLD, Khoo MCK, Nayak KS. Real-time 3D magnetic resonance imaging of the pharyngeal airway in sleep apnea. Magn Reson Med. 2014;71(4):1501–10.
45. Sabati M, Lauzon ML, Nagarajappa N, Frayne R. A real-time 3D large field-of-view MRI system with interactive table motion. Concepts Magn Reson Part B Magn Reson Eng. 2006;29B(1):28–41.
46. Riederer SJ, Tasciyan T, Farzaneh F, Lee JN, Wright RC, Herfkens RJ. MR fluoroscopy: Technical feasibility. Magn Reson Med. 1988;8(1):1–15.
47. Pruessmann KP, Weiger M, Scheidegger MB, Boesiger P. SENSE: sensitivity encoding for fast MRI. Magn Reson Med. 1999;42(5):952–62.
48. Griswold MA, Jakob PM, Heidemann RM, Nittka M, Jellus V, Wang J, et al. Generalized autocalibrating partially parallel acquisitions (GRAPPA). Magn Reson Med. 2002;47(6):1202–10.
49. O'Sullivan JD. A fast sinc function gridding algorithm for Fourier inversion in computer tomography. IEEE Trans Med Imaging. 1985;4(4):200–7.
50. Pruessmann KP, Weiger M, Börnert P, Boesiger P. Advances in sensitivity encoding with arbitrary k-space trajectories. Magn Reson Med. 2001;46(4):638–51.

51. Seiberlich N, Breuer FA, Blaimer M, Barkauskas K, Jakob PM, Griswold MA. Non-Cartesian data reconstruction using GRAPPA operator gridding (GROG). Magn Reson Med. 2007;58(6):1257–65.

52. Seiberlich N, Griswold M. Self-calibrating through-time spiral GRAPPA for real-time CMR. J Cardiovasc Magn Reson. 2013;15(1):E28.

53. Seiberlich N, Ehses P, Duerk J, Gilkeson R, Griswold M. Improved radial GRAPPA calibration for real-time free-breathing cardiac imaging. Magn Reson Med. 2011;65(2):492–505.

54. Lingala SG, Zhu Y, Lim Y, Toutios A, Ji Y, Lo W, et al. Feasibility of through-time spiral generalized autocalibrating partial parallel acquisition for low latency accelerated real-time MRI of speech. Magn Reson Med. 2017;78:2275–82.

55. Ruthven M, Freitas AC, Boubertakh R, Miquel ME. Application of radial GRAPPA techniques to single- and multislice dynamic speech MRI using a 16-channel neurovascular coil. Magn Reson Med. 2019;82(3):948–58.

56. Huang F, Akao J, Vijayakumar S, Duensing GR, Limkeman M. k-t GRAPPA: a k-space implementation for dynamic MRI with high reduction factor. Magn Reson Med. 2005;54(5):1172–84.

57. Ponce IP, Blaimer M, Breuer FA, Griswold MA, Jakob PM, Kellman P. Auto-calibration approach for k–t SENSE. Magn Reson Med. 2014;71(3):1123–9.

58. Liang Z-P, Boada F, Constable R, Haacke E, Lauterbur P, Smith M. Constrained reconstruction methods in MR Imaging. Rev Magn Reson Med. 1992;4:67–185.

59. Lustig M, Donoho DL, Santos JM, Pauly JM. Compressed sensing MRI. IEEE Signal Process Mag. 2008;25(2):72–82.

60. Müller S, Umathum R, Speier P, Zühlsdorff S, Ley S, Semmler W, et al. Dynamic coil selection for real-time imaging in interventional MRI. Magn Reson Med. 2006;56(5):1156–62.

61. Buehrer M, Pruessmann KP, Boesiger P, Kozerke S. Array compression for MRI with large coil arrays. Magn Reson Med. 2007;57(6):1131–9.

62. Kowalik GT, Steeden JA, Pandya B, Odille F, Atkinson D, Taylor A, et al. Real-time flow with fast GPU reconstruction for continuous assessment of cardiac output. J Magn Reson Imaging. 2012;36(6):1477–82.

63. Sorensen TS, Atkinson D, Schaeffter T, Hansen MS. Real-Time Reconstruction of Sensitivity Encoded Radial Magnetic Resonance Imaging Using a Graphics Processing Unit. IEEE Trans Med Imaging. 2009;28(12):1974–85.

64. Schaetz S, Uecker M. A multi-GPU programming library for real-time applications. In: Proceedings of the 12th International Conference on Algorithms and Architectures for Parallel Processing - Volume Part I. 2012. p. 114–28.

65. Smith DS, Gore JC, Yankeelov TE, Welch EB. Real-Time compressive sensing MRI reconstruction using GPU computing and split bregman methods. Int J Biomed Imaging. 2012;2012:864827.

66. Bernstein MA, Zhou XJ, Polzin JA, King KF, Ganin A, Pelc NJ, et al. Concomitant gradient terms in phase contrast MR: Analysis and correction. Magn Reson Med. 1998;39(2):300–8.

67. King KF, Ganin A, Zhou XJ, Bernstein MA. Concomitant gradient field effects in spiral scans. Magn Reson Med. 1999;41(1):103–12.

68. Cheng JY, Santos JM, Pauly JM. Fast concomitant gradient field and field inhomogeneity correction for spiral cardiac imaging. Magn Reson Med. 2011;66(2):390–401.

69. Barmet C, Zanche N De, Pruessmann KP. Spatiotemporal magnetic field monitoring for MR. Magn Reson Med. 2008;60(1):187–97.

70. De Zanche N, Barmet C, Nordmeyer-Massner JA, Pruessmann KP. NMR probes for measuring magnetic fields and field dynamics in MR systems. Magn Reson Med. 2008;60(1):176–86.

71. Wilm BJ, Barmet C, Pavan M, Pruessmann KP. Higher order reconstruction for MRI in the presence of spatiotemporal field perturbations. Magn Reson Med. 2011;65(6):1690–701.

72. https://github.com/ismrmrd/ismrmrd.

73. https://github.com/davidssmith/RawArray.jl.

74. Ravi KS, Potdar S, Poojar P, Reddy AK, Kroboth S, Nielsen J-F, et al. Pulseq-graphical programming interface: open source visual environment for prototyping pulse sequences and integrated magnetic resonance imaging algorithm development. Magn Reson Imaging. 2018;52:9–15.

75. Barber NJ, Ako EO, Kowalik GT, Cheang MH, Pandya B, Steeden JA, et al. Magnetic

resonance–augmented cardiopulmonary exercise testing. Circ Cardiovasc Imaging. 2016;9(12):e005282.

76. Barral JK, Overall WR, Nystrom MM, Feng X, Reeve Ingle R, Johnson KO, et al. A novel platform for comprehensive CMR examination in a clinically feasible scan time. J Cardiovasc Magn Reson. 2014;16(Suppl 1):W10.

77. Lim Y, Narayanan S, Nayak KS. Deblurring for spiral real-time MRI using convolutional neural networks. Magn Reson Med. 2020;84:3438–3452.

78. Kakareka JW, Faranesh AZ, Pursley RH, Campbell-Washburn A, Herzka DA, Rogers T, et al. Physiological recording in the MRI environment (PRiME): MRI-compatible hemodynamic recording system. IEEE J Transl Eng Heal Med. 2018;6:4100112.

79. Rogers T, Ratnayaka K, Khan JM, Stine A, Schenke WH, Grant LP, et al. CMR fluoroscopy right heart catheterization for cardiac output and pulmonary vascular resistance: results in 102 patients. J Cardiovasc Magn Reson. 2017;19(1):54.

80. Inouye JM, Blemker SS, Inouye DI. Towards undistorted and noise-free speech in an MRI scanner: correlation subtraction followed by spectral noise gating. J Acoust Soc Am. 2014;135(3):1019–22.

81. Santos JM, Wright GA, Pauly JM. Flexible real-time magnetic resonance imaging framework. Conf Proc IEEE Eng Med Biol Soc. 2004:1048–51.

82. Guttman MA, Lederman RJ, Sorger JM, McVeigh ER. Real-time volume rendered MRI for interventional guidance. J Cardiovasc Magn Reson. 2002;4(4):431–42.

83. Hatscher B, Mewes A, Pannicke E, Kägebein U, Wacker F, Hansen C, et al. Touchless scanner control to support MRI-guided interventions. Int J Comput Assist Radiol Surg. 2020;15(3):545–53.

84. Mewes A, Heinrich F, Hensen B, Wacker F, Lawonn K, Hansen C. Concepts for augmented reality visualisation to support needle guidance inside the MRI. Healthc Technol Lett. 2018;5(5):172–6.

85. Unterberg-Buchwald C, Fasshauer M, Sohns JM, Staab W, Schuster A, Voit D, et al. Real time cardiac MRI and its clinical usefulness in arrhythmias and wall motion abnormalities. J Cardiovasc Magn Reson. 2014;16(1):P34.

86. Allen BD, Carr ML, Markl M, Zenge MO, Schmidt M, Nadar MS, et al. Accelerated real-time cardiac MRI using iterative sparse SENSE reconstruction: comparing performance

in patients with sinus rhythm and atrial fibrillation. Eur Radiol. 2018;28(7):3088–96.

87. Ahmad R, Hu HH, Krishnamurthy R, Krishnamurthy R. Reducing sedation for pediatric body MRI using accelerated and abbreviated imaging protocols. Pediatr Radiol. 2018;48(1):37–49.

88. Setser RM, Fischer SE, Lorenz CH. Quantification of left ventricular function with magnetic resonance images acquired in real time. J Magn Reson Imaging. 2000;12(3):430–8.

89. Muthurangu V, Lurz P, Critchely JD, Deanfield JE, Taylor AM, Hansen MS. Real-time assessment of right and left ventricular volumes and function in patients with congenital heart disease by using high spatiotemporal resolution radial k-t SENSE. Radiology. 2008;248(3):782–91.

90. Haji-Valizadeh H, Rahsepar AA, Collins JD, Bassett E, Isakova T, Block T, et al. Validation of highly accelerated real-time cardiac cine MRI with radial k-space sampling and compressed sensing in patients at 1.5T and 3T. Magn Reson Med. 2018;79(5):2745–51.

91. Voit D, Zhang S, Unterberg-Buchwald C, Sohns JM, Lotz J, Frahm J. Real-time cardiovascular magnetic resonance at 1.5 T using balanced SSFP and 40 ms resolution. J Cardiovasc Magn Reson. 2013;15(1):79.

92. Hauptmann A, Arridge S, Lucka F, Muthurangu V, Steeden JA. Real-time cardiovascular MR with spatio-temporal artifact suppression using deep learning–proof of concept in congenital heart disease. Magn Reson Med. 2019;81(2):1143–56.

93. Steeden JA, Kowalik GT, Tann O, Hughes M, Mortensen KH, Muthurangu V. Real-time assessment of right and left ventricular volumes and function in children using high spatiotemporal resolution spiral bSSFP with compressed sensing. J Cardiovasc Magn Reson. 2018;20(1):79.

94. Tang C, Blatter DD, Parker DL. Accuracy of phase-contrast flow measurements in the presence of partial-volume effects. J Magn Reson Imaging. 1993;3(2):377–85.

95. Gabbert DD, Hart C, Jerosch-Herold M, Wegner P, Salehi Ravesh M, Voges I, et al. Heart beat but not respiration is the main driving force of the systemic venous return in the Fontan circulation. Sci Rep. 2019;9(1):2034.

96. Körperich H, Müller K, Barth P, Gieseke J, Haas N, Schulze-Neick I, et al. Differentiation of impaired from preserved hemodynamics in patients with fontan circulation using

real-time phase-velocity cardiovascular magnetic resonance. J Thorac Imaging. 2017;32(3).

97. Hermann K, Jürgen G, Peter B, Romhild H, Hermann E, Andreas P, et al. Flow volume and shunt quantification in pediatric congenital heart disease by real-time magnetic resonance velocity mapping. Circulation. 2004;109(16):1987–93.

98. Kowallick JT, Joseph AA, Unterberg-Buchwald C, Fasshauer M, van Wijk K, Merboldt KD, et al. Real-time phase-contrast flow MRI of the ascending aorta and superior vena cava as a function of intrathoracic pressure (Valsalva manoeuvre). Br J Radiol. 2014;87(1042):20140401.

99. Kowalik GT, Knight D, Steeden JA, Muthurangu V. Perturbed spiral real-time phase-contrast MR with compressive sensing reconstruction for assessment of flow in children. Magn Reson Med. 2020;83(6):2077–91.

100. Singh JP, Larson MG, Manolio TA, O'Donnell CJ, Lauer M, Evans JC, et al. Blood pressure response during treadmill testing as a risk factor for new-onset hypertension. Circulation. 1999;99(14):1831–6.

101. Lurz P, Muthurangu V, Schuler PK, Giardini A, Schievano S, Nordmeyer J, et al. Impact of reduction in right ventricular pressure and/or volume overload by percutaneous pulmonary valve implantation on biventricular response to exercise: an exercise stress real-time CMR study. Eur Heart J. 2012;33(19):2434–41.

102. O'Meagher S, Munoz PA, Muthurangu V, Robinson PJ, Malitz N, Tanous DJ, et al. Mechanisms of maintained exercise capacity in adults with repaired tetralogy of Fallot. Int J Cardiol. 2014;177(1):178–81.

103. Jaijee S, Quinlan M, Tokarczuk P, Clemence M, Howard LSGE, Gibbs JSR, et al. Exercise cardiac MRI unmasks right ventricular dysfunction in acute hypoxia and chronic pulmonary arterial hypertension. Am J Physiol Circ Physiol. 2018;315(4):H950–7.

104. Hjortdal VE, Emmertsen K, Stenbøg E, Fründ T, Schmidt MR, Kromann O, et al. Effects of exercise and respiration on blood flow in total cavopulmonary connection. Circulation. 2003;108(10):1227–31.

105. Pedersen LM, Pedersen TAL, Pedersen EM, Højmyr H, Emmertsen K, Hjortdal VE. Blood flow measured by magnetic resonance imaging at rest and exercise after surgical bypass of aortic arch obstruction☆. Eur J Cardio-Thoracic Surg. 2010;37(3):658–61.

106. Barber NJ, Ako EO, Kowalik GT, Steeden JA, Pandya B, Muthurangu V. MR augmented cardiopulmonary exercise testing—a novel approach to assessing cardiovascular function. Physiol Meas. 2015;36(5):N85–94.

107. Manganaro L, Savelli S, Di Maurizio M, Perrone A, Tesei J, Francioso A, et al. Potential role of fetal cardiac evaluation with magnetic resonance imaging: preliminary experience. Prenat Diagn. 2008;28(2):148–56.

108. Roy CW, van Amerom JFP, Marini D, Seed M, Macgowan CK. Fetal cardiac MRI: a review of technical advancements. Top Magn Reson Imaging. 2019;28(5):235–244.

109. Roy CW, Seed M, Kingdom JC, Macgowan CK. Motion compensated cine CMR of the fetal heart using radial undersampling and compressed sensing. J Cardiovasc Magn Reson. 2017;19(1):29.

110. Mukherjee RK, Chubb H, Roujol S, Razavi R, O'Neill MD. Advances in real-time MRI-guided electrophysiology. Curr Cardiovasc Imaging Rep. 2019;12(2):6.

111. Campbell-Washburn AE, Tavallaei MA, Pop M, Grant EK, Chubb H, Rhode K, et al. Real-time MRI guidance of cardiac interventions. J Magn Reson Imaging. 2017;46(4):935–50.

112. Campbell-Washburn AE, Faranesh AZ, Lederman RJ, Hansen MS. Magnetic resonance sequences and rapid acquisition for MR-guided interventions. Magn Reson Imaging Clin N Am. 2015;23(4):669–79.

113. Penzkofer T, Tuncali K, Fedorov A, Song S-E, Tokuda J, Fennessy FM, et al. Transperineal in-bore 3-T MR imaging-guided prostate biopsy: a prospective clinical observational study. Radiology. 2014;274(1):170–80.

114. van den Bosch MAAJ, Daniel BL, Pal S, Nowels KW, Birdwell RL, Jeffrey SS, et al. MRI-guided needle localization of suspicious breast lesions: results of a freehand technique. Eur Radiol. 2006;16(8):1811–7.

115. Mittauer K, Paliwal B, Hill P, Bayouth JE, Geurts MW, Baschnagel AM, et al. A new era of image guidance with magnetic resonance-guided radiation therapy for abdominal and thoracic malignancies. Cureus. 2018;10(4):e2422–e2422.

116. van den Bosch M, Daniel B, Rieke V, Butts-Pauly K, Kermit E, Jeffrey S. MRI-guided radiofrequency ablation of breast cancer: Preliminary clinical experience. J Magn Reson Imaging. 2008;27(1):204–8.

117. Lewin JS, Nour SG, Connell CF, Sulman A, Duerk JL, Resnick MI, et al. Phase II clinical trial of interactive MR imaging–guided interstitial radiofrequency thermal ablation of primary kidney tumors: initial experience. Radiology. 2004;232(3):835–45.

118. Woodrum DA, Kawashima A, Gorny KR, Mynderse LA. Magnetic resonance-guided thermal therapy for localized and recurrent prostate cancer. Magn Reson Imaging Clin N Am. 2015;23(4):607–19.

119. Zippel DB, Papa MZ. The use of MR imaging guided focused ultrasound in breast cancer patients; a preliminary phase one study and review. Breast Cancer. 2005;12(1):32–8.

120. Grothoff M, Piorkowski C, Eitel C, Gaspar T, Lehmkuhl L, Lücke C, et al. MR imaging–guided electrophysiological ablation studies in humans with passive catheter tracking: initial results. Radiology. 2014;271(3):695–702.

121. Sommer P, Grothoff M, Eitel C, Gaspar T, Piorkowski C, Gutberlet M, et al. Feasibility of real-time magnetic resonance imaging-guided electrophysiology studies in humans. EP Eur. 2012;15(1):101–8.

122. Chubb H, Harrison JL, Weiss S, Krueger S, Koken P, Bloch LØ, et al. Development, preclinical validation, and clinical translation of a cardiac magnetic resonance - electrophysiology system with active catheter tracking for ablation of cardiac arrhythmia. JACC Clin Electrophysiol. 2017;3(2):89–103.

123. Ratnayaka K, Kanter JP, Faranesh AZ, Grant EK, Olivieri LJ, Cross RR, et al. Radiation-free CMR diagnostic heart catheterization in children. J Cardiovasc Magn Reson. 2017;19(1):65.

124. Pushparajah K, Tzifa A, Razavi R. Cardiac MRI catheterization: A 10-year single institution experience and review. Interv Cardiol. 2014;6(3):335–346.

125. Sonmez M, Saikus CE, Bell JA, Franson DN, Halabi M, Faranesh AZ, et al. MRI active guidewire with an embedded temperature probe and providing a distinct tip signal to enhance clinical safety. J Cardiovasc Magn Reson. 2012;14(1):38.

126. Dumoulin CL, Souza SP, Darrow RD. Real-time position monitoring of invasive devices using magnetic resonance. Magn Reson Med. 1993;29(3):411–5.

127. Sathyanarayana S, Schär M, Kraitchman DL, Bottomley PA. Towards real-time intravascular endoscopic magnetic resonance imaging. JACC Cardiovasc Imaging. 2010;3(11):1158–65.

128. Scheer JK, Hamelin T, Chang L, Lemkuil B, Carter BS, Chen CC. Real-time magnetic resonance imaging-guided biopsy using SmartFrame® stereotaxis in the setting of a conventional diagnostic magnetic resonance imaging suite. Oper Neurosurg. 2017;13(3):329–37.

129. Moche M, Heinig S, Garnov N, Fuchs J, Petersen T-O, Seider D, et al. Navigated MRI-guided liver biopsies in a closed-bore scanner: experience in 52 patients. Eur Radiol. 2016;26(8):2462–70.

130. Overduin CG, Heidkamp J, Rothgang E, Barentsz JO, de Lange F, Fütterer JJ. Fast 3-T MR-guided transrectal prostate biopsy using an in-room tablet device for needle guide alignment: a feasibility study. Eur Radiol. 2018;28(11):4824–31.

131. Heidt T, Reiss S, Krafft AJ, Özen AC, Lottner T, Hehrlein C, et al. Real-time magnetic resonance imaging - guided coronary intervention in a porcine model. Sci Rep. 2019;9(1):8663.

132. Campbell-Washburn AE, Rogers T, Stine AM, Khan JM, Ramasawmy R, Schenke WH, et al. Right heart catheterization using metallic guidewires and low SAR cardiovascular magnetic resonance fluoroscopy at 1.5 Tesla: first in human experience. J Cardiovasc Magn Reson. 2018;20(1):41.

133. Unterberg-Buchwald C, Ritter CO, Reupke V, Wilke RN, Stadelmann C, Steinmetz M, et al. Targeted endomyocardial biopsy guided by real-time cardiovascular magnetic resonance. J Cardiovasc Magn Reson. 2017;19(1):45.

134. Toupin S, Bour P, Lepetit-Coiffé M, Ozenne V, Denis de Senneville B, Schneider R, et al. Feasibility of real-time MR thermal dose mapping for predicting radiofrequency ablation outcome in the myocardium in vivo. J Cardiovasc Magn Reson. 2017;19(1):14.

135. Ozenne V, Toupin S, Bour P, de Senneville BD, Lepetit-Coiffé M, Boissenin M, et al. Improved cardiac magnetic resonance thermometry and dosimetry for monitoring lesion formation during catheter ablation. Magn Reson Med. 2017;77(2):673–83.

136. Kim T, Park JC, Gach HM, Chun J, Mutic S. Technical note: real-time 3D MRI in the presence of motion for MRI-guided radiotherapy: 3D dynamic keyhole imaging with super-resolution. Med Phys. 2019;46(10):4631–8.

137. Chen W, Byrd D, Narayanan S, Nayak KS. Intermittently tagged real-time MRI reveals internal tongue motion during speech production. Magn Reson Med. 2019;82(2):600–

13.

138. Chen W, Lee NG, Byrd D, Narayanan S, Nayak KS. Improved real-time tagged MRI using REALTAG. Magn Reson Med. 2020;84(2):838–46.
139. Zhu Y, Kim YC, Proctor MI, Narayanan SS, Nayak KS. Dynamic 3-D visualization of vocal tract shaping during speech. IEEE Trans Med Imaging. 2013;32(5):838–48.
140. Engwall O. From real-time MRI to 3D tongue movements. Interspeech. 2004.
141. Scott AD, Wylezinska M, Birch MJ, Miquel ME. Speech MRI: morphology and function. Phys Medica. 2014;30(6):604–18.
142. Nayak KS, Fleck RJ. Seeing sleep: dynamic imaging of upper airway collapse and collapsibility in children. IEEE Pulse. 2014;5(5):40–4.
143. Zu Y, Narayanan SS, Kim Y-C, Nayak K, Bronson-Lowe C, Villegas B, et al. Evaluation of swallow function after tongue cancer treatment using real-time magnetic resonance imaging: a pilot study. JAMA Otolaryngol Head Neck Surg. 2013;139(12):1312–9.
144. Bresch E, Nielsen J, Nayak K, Narayanan S. Synchronized and noise-robust audio recordings during realtime magnetic resonance imaging scans. J Acoust Soc Am. 2006;120(4):1791–4.
145. Olthoff A, Joseph AA, Weidenmüller M, Riley B, Frahm J. Real-time MRI of swallowing: intraoral pressure reduction supports larynx elevation. NMR Biomed. 2016;29(11):1618–23.
146. Tian W, Li Y, Yin H, Zhao S-F, Li S, Wang Y, et al. Magnetic resonance imaging assessment of velopharyngeal motion in chinese children after primary palatal repair. J Craniofac Surg. 2010;21(2).
147. Hagedorn C, Lammert A, Zu Y, Sinha U, Goldstein L, Narayanan SS. Characterizing post-glossectomy speech using real-time magnetic resonance imaging. J Acoust Soc Am. 2013;134(5):4205.
148. Mady K, Sader R, Beer A, Hoole P, Zimmermann A, Hannig C. Consonant articulation in glossectomee speech evaluated by dynamic MRI. In: Proceedings of the Fifteenth International Congress of Phonetic Sciences (ICPhS). 2015. p. 3233–3236.
149. Bae Y, Kuehn DP, Conway CA, Sutton BP. Real-time magnetic resonance imaging of velopharyngeal activities with simultaneous speech recordings. Cleft Palate-Craniofacial J. 2011;48(6):695–707.

150. Kazan-Tannus JF, Levine D, McKenzie C, Lim K-H, Cohen B, Farrar N, et al. Real-time magnetic resonance imaging aids prenatal diagnosis of isolated cleft palate. J Ultrasound Med. 2005;24(11):1533–40.

151. Bresch E, Kim Y-C, Nayak K, Byrd D, Narayanan S. Seeing speech: Capturing vocal tract shaping using real-time magnetic resonance imaging [Exploratory DSP]. IEEE Signal Process Mag. 2008;25(3):123–32.

152. Kim Y-C. Fast upper airway magnetic resonance imaging for assessment of speech production and sleep apnea. Precis Futur Med. 2018;2(4):131–48.

153. Ramanarayanan V, Tilsen S, Proctor M, Töger J, Goldstein L, Nayak KS, et al. Analysis of speech production real-time MRI. Computer Speech and Language. 2018;52:1–22.

154. Zhang S, Joseph AA, Gross L, Ghadimi M, Frahm J, Beham AW. Diagnosis of gastroesophageal reflux disease using real-time magnetic resonance imaging. Sci Rep. 2015;5(1):12112.

155. Freitas AC, Ruthven M, Boubertakh R, Miquel ME. Real-time speech MRI: commercial Cartesian and non-Cartesian sequences at 3T and feasibility of offline TGV reconstruction to visualise velopharyngeal motion. Phys Medica. 2018;46:96–103.

156. Uecker M, Zhang S, Voit D, Karaus A, Merboldt KD, Frahm J. Real-time MRI at a resolution of 20 ms. NMR Biomed. 2010;23(8):986–94.

157. Niebergall A, Zhang S, Kunay E, Keydana G, Job M, Uecker M, et al. Real-time MRI of speaking at a resolution of 33 ms: Undersampled radial FLASH with nonlinear inverse reconstruction. Magn Reson Med. 2013;69(2):477–85.

158. Iltis PW, Frahm J, Voit D, Joseph AA, Schoonderwaldt E, Altenmüller E. High-speed real-time magnetic resonance imaging of fast tongue movements in elite horn players. Quant Imaging Med Surg. 2015;5(3):374–81.

159. Sutton BP, Conway CA, Bae Y, Seethamraju R, Kuehn DP. Faster dynamic imaging of speech with field inhomogeneity corrected spiral fast low angle shot (FLASH) at 3 T. J Magn Reson Imaging. 2010;32(5):1228–37.

160. Lim Y, Lingala SG, Narayanan SS, Nayak KS. Dynamic off-resonance correction for spiral real-time MRI of speech. Magn Reson Med. 2019;81(1):234–46.

161. Feng X, Blemker SS, Inouye J, Pelland CM, Zhao L, Meyer CH. Assessment of velopharyngeal function with dual-planar high-resolution real-time spiral dynamic MRI.

Magn Reson Med. 2018;80:1467–74.

162. Borotikar B, Lempereur M, Lelievre M, Burdin V, Ben Salem D, Brochard S. Dynamic MRI to quantify musculoskeletal motion: a systematic review of concurrent validity and reliability, and perspectives for evaluation of musculoskeletal disorders. PLoS One. 2017;12(12):e0189587–e0189587.

163. d'Entremont AG, Nordmeyer-Massner JA, Bos C, Wilson DR, Pruessmann KP. Do dynamic-based MR knee kinematics methods produce the same results as static methods? Magn Reson Med. 2013;69(6):1634–44.

164. Kaiser J, Bradford R, Johnson K, Wieben O, Thelen DG. Measurement of tibiofemoral kinematics using highly accelerated 3D radial sampling. Magn Reson Med. 2013;69(5):1310–6.

165. Mazzoli V, Oudeman J, Nicolay K, Maas M, Verdonschot N, Sprengers AM, et al. Assessment of passive muscle elongation using diffusion tensor MRI: correlation between fiber length and diffusion coefficients. NMR Biomed. 2016;29(12):1813–24.

166. Deligianni X, Pansini M, Garcia M, Hirschmann A, Schmidt-Trucksäss A, Bieri O, et al. Synchronous MRI of muscle motion induced by electrical stimulation. Magn Reson Med. 2017;77(2):664–72.

167. Westphal CJ, Schmitz A, Reeder SB, Thelen DG. Load-dependent variations in knee kinematics measured with dynamic MRI. J Biomech. 2013;46(12):2045–52.

168. Quick HH, Ladd ME, Hoevel M, Bosk S, Debatin JF, Laub G, et al. Real-time MRI of joint movement with trueFISP. J Magn Reson Imaging. 2002;15(6):710–5.

169. Mazzoli V, Nederveen AJ, Oudeman J, Sprengers A, Nicolay K, Strijkers GJ, et al. Water and fat separation in real-time MRI of joint movement with phase-sensitive bSSFP. Magn Reson Med. 2017;78(1):58–68.

170. Tan Z, Voit D, Kollmeier JM, Uecker M, Frahm J. Dynamic water/fat separation and inhomogeneity mapping—joint estimation using undersampled triple-echo multi-spoke radial FLASH. Magn Reson Med. 2019;82(3):1000–11.

171. Draper CE, Santos JM, Kourtis LC, Besier TF, Fredericson M, Beaupre GS, et al. Feasibility of using real-time MRI to measure joint kinematics in 1.5T and open-bore 0.5T systems. J Magn Reson Imaging. 2008;28(1):158–66.

172. Draper CE, Besier TF, Santos JM, Jennings F, Fredericson M, Gold GE, et al. Using real-

time MRI to quantify altered joint kinematics in subjects with patellofemoral pain and to evaluate the effects of a patellar brace or sleeve on joint motion. J Orthop Res. 2009;27(5):571–7.

173. Draper CE, Besier TF, Fredericson M, Santos JM, Beaupre GS, Delp SL, et al. Differences in patellofemoral kinematics between weight-bearing and non-weight-bearing conditions in patients with patellofemoral pain. J Orthop Res. 2011;29(3):312–7.
174. Lin C-C, Zhang S, Hsu C-Y, Frahm J, Lu T-W, Shih T-F. Measuring three-dimensional tibiofemoral kinematics using dual-slice real-time magnetic resonance imaging. Med Phys. 2019;46(10):4588–99.
175. Lin C-C, Zhang S, Frahm J, Lu T-W, Hsu C-Y, Shih T-F. A slice-to-volume registration method based on real-time magnetic resonance imaging for measuring three-dimensional kinematics of the knee. Med Phys. 2013;40(10):102302.
176. Kawchuk GN, Fryer J, Jaremko JL, Zeng H, Rowe L, Thompson R. Real-time visualization of joint cavitation. PLoS One. 2015;10(4):e0119470–e0119470.
177. Shaw CB, Foster BH, Borgese M, Boutin RD, Bateni C, Boonsri P, et al. Real-time three-dimensional MRI for the assessment of dynamic carpal instability. PLoS One. 2019;14(9):e0222704–e0222704.
178. Henrichon SS, Foster BH, Shaw C, Bayne CO, Szabo RM, Chaudhari AJ, et al. Dynamic MRI of the wrist in less than 20 seconds: normal midcarpal motion and reader reliability. Skeletal Radiol. 2020;49(2):241–8.
179. Tempelaere C, Pierrart J, Lefèvre-Colau M-M, Vuillemin V, Cuénod C-A, Hansen U, et al. Dynamic three-dimensional shoulder MRI during active motion for investigation of rotator cuff diseases. PLoS One. 2016;11(7):e0158563–e0158563.
180. Krohn S, Gersdorff N, Wassmann T, Merboldt K-D, Joseph AA, Buergers R, et al. Real-time MRI of the temporomandibular joint at 15 frames per second—A feasibility study. Eur J Radiol. 2016;85(12):2225–30.
181. Yen P, Katzberg RW, Buonocore MH, Sonico J. Dynamic MR imaging of the temporomandibular joint using a balanced steady-state free precession sequence at 3T. Am J Neuroradiol. 2013;34(3):E24 LP-E26.
182. Menys A, Taylor SA, Emmanuel A, Ahmed A, Plumb AA, Odille F, et al. Global small bowel motility: assessment with dynamic MR imaging. Radiology. 2013;269(2):443–50.

183. de Jonge CS, Coolen BF, Peper ES, Motaal AG, Nio CY, Somers I, et al. Evaluation of compressed sensing MRI for accelerated bowel motility imaging. Eur Radiol Exp. 2019;3(1):7.

184. Seif Amir Hosseini A, Uhlig J, Streit U, Voit D, Uhlig A, Ellenrieder V, et al. Real-time MRI for the dynamic assessment of fundoplication failure in patients with gastroesophageal reflux disease. Eur Radiol. 2019;29(9):4691–8.

185. Rai R, Sidhom M, Lim K, Ohanessian L, Liney GP. MRI micturating urethrography for improved urethral delineation in prostate radiotherapy planning: a case study. Phys Med Biol. 2017;62(8):3003–10.

186. Maccioni F. Functional disorders of the ano-rectal compartment of the pelvic floor: clinical and diagnostic value of dynamic MRI. Abdom Imaging. 2013;38(5):930–51.

187. Maccioni F, Alt CD. MRI of the pelvic floor and MR defecography. In: Hodler J, Kubik-Huch RA, von Schulthess GK (eds). Diseases of the Abdomen and Pelvis 2018-2021. IDKD Springer Series, Springer, Cham. 2018. p. 13–20.

188. Kubik-Huch RA, Wisser J, Stallmach T, Ladd ME, Meier A, Marincek B. Prenatal diagnosis of fetal malformations by ultrafast magnetic resonance imaging. Prenat Diagn. 1998;18(11):1205–8.

189. Guo W-Y, Wong T-T. Screening of fetal CNS anomalies by MR imaging. Child's Nerv Syst. 2003;19(7):410–4.

190. Levine D, Cavazos C, Kazan-Tannus JF, McKenzie CA, Dialani V, Robson CD, et al. Evaluation of real-time single-shot fast spin-echo MRI for visualization of the fetal midline corpus callosum and secondary palate. Am J Roentgenol. 2006;187(6):1505–11.

191. Yankeelov TE, Gore JC. Dynamic contrast enhanced magnetic resonance imaging in oncology: theory, data acquisition, analysis, and examples. Curr Med Imaging Rev. 2009;3(2):91–107.

192. Riederer SJ, Haider CR, Borisch EA, Weavers PT, Young PM. Recent advances in 3D time-resolved contrast-enhanced MR angiography. J Magn Reson Imaging. 2015;42(1):3–22.

193. van Osch MJP, Teeuwisse WM, Chen Z, Suzuki Y, Helle M, Schmid S. Advances in arterial spin labelling MRI methods for measuring perfusion and collateral flow. J Cereb Blood Flow Metab. 2017;38(9):1461–80.

194. Hennig J, Zhong K, Speck O. MR-Encephalography: Fast multi-channel monitoring of brain physiology with magnetic resonance. Neuroimage. 2007;34(1):212–9.

195. Zhou Z, Han F, Ghodrati V, Gao Y, Yin W, Yang Y, et al. Parallel imaging and convolutional neural network combined fast MR image reconstruction: applications in low-latency accelerated real-time imaging. Med Phys. 2019;46(8):3399–413.

196. Han F, Zhou Z, Kouzehkonan VG, Gao Y, Yang Y, Hu P. Single breath-held, ECG-free cardiac CINE MRI using parallel imaging and deep learning combined image reconstruction. In: Proceedings of the 27th Annual Meeting of ISMRM, Montréal, QC, Canada. 2019. p. 1048.

197. Dietz B, Fallone G, Wachowicz K. Real-time MR image reconstruction using convolutional neural networks. In: Proceedings of the 27th Annual Meeting of ISMRM, Montréal, QC, Canada. 2019. p. 4784.

198. Alkan C, Fang Z, Lee JH. Convolutional neural network for real-time high spatial resolution functional magnetic resonance imaging. In: Proceedings of the 27th Annual Meeting of ISMRM, Montréal, QC, Canada. 2019. p. 4792.

199. Saha P, Srungarapu P, Fels S. Towards automatic speech identification from vocal tract shape dynamics in real-time MRI. In: Proc Interspeech. 2018. p. 1249–1253.

200. Leeuwen KG van, Bos P, Trebeschi S, Alphen MJA van, Voskuilen L, Smeele LE, et al. CNN-based phoneme classifier from vocal tract MRI learns embedding consistent with articulatory topology. In: Proc Interspeech. 2019. p. 909–913.

201. Somandepalli K, Toutios A, Narayanan SS. Semantic edge detection for tracking vocal tract air-Tissue boundaries in real-Time magnetic resonance images. In: Proc Interspeech. 2017. p. 631–635.

202. Valliappan CA, Mannem R, Ghosh PK. Air-tissue boundary segmentation in real-time magnetic resonance imaging video using semantic segmentation with fully convolutional networks. In: Proc Interspeech. 2018. p. 3132–3136.

203. Yang F, Zhang Y, Lei P, Wang L, Miao Y, Xie H, et al. A deep learning segmentation approach in free-breathing real-time cardiac magnetic resonance imaging. Biomed Res Int. 2019;2019:5636423.

204. Weine J, Breton E, Garnon J, Gangi A, Maier F. Deep learning based needle localization on real-time MR images of patients acquired during MR-guided percutaneous

interventions. In: Proceedings of the 27th Annual Meeting of ISMRM, Montréal, QC, Canada. 2019. p. 0973.

205. Li X, Young AS, Raman SS, Lu DS, Lee Y-H, Tsao T-C, et al. Automatic needle tracking using Mask R-CNN for MRI-guided percutaneous interventions. Int J Comput Assist Radiol Surg. 2020;15:1673–1684.
206. Krishnamurthy D, You W, Kapse K, Limperopoulos C. Real-time ultrafast fetal brain localization using convolutional neural networks. In: Proceedings of the 27th Annual Meeting of ISMRM, Montréal, QC, Canada. 2019. p. 4810.
207. Kim J-M, Jeong Y-J, Cheong H-J, Yoo J-W, Kim J-H, Lee C, et al. Real-time T1/PRF-based MR thermometry using deep learning and VFA-mFFE for guidance of HIFU treatment. In: Proceedings of the 27th Annual Meeting of ISMRM, Montréal, QC, Canada. 2019. p. 0970.
208. https://www.heartvista.ai/technology.
209. https://www.mevis.fraunhofer.de/en/solutionpages/deep-learning-in-medical-imaging.html.
210. Campbell-Washburn AE, Ramasawmy R, Restivo MC, Bhattacharya I, Basar B, Herzka DA, et al. Opportunities in interventional and diagnostic imaging by using high-performance low-field-strength MRI. Radiology. 2019;293(2):384–93.
211. Konings MK, Bartels LW, Smits HFM, Bakker CJG. Heating around intravascular guidewires by resonating RF waves. J Magn Reson Imaging. 2000;12(1):79–85.
212. Wald LL, McDaniel PC, Witzel T, Stockmann JP, Cooley CZ. Low-cost and portable MRI. J Magn Reson Imaging. 2020;52:686–696.
213. Fiorentino NM, Lin JS, Ridder KB, Guttman MA, McVeigh ER, Blemker SS. Rectus femoris knee muscle moment arms measured in vivo during dynamic motion with real-time magnetic resonance imaging. J Biomech Eng. 2013;135(4).
214. Lingala SG, Toutios A, Toger J, Lim Y, Zhu Y, Kim YC, et al. State-of-the-art MRI protocol for comprehensive assessment of vocal tract structure and function. In: Proc Interspeech. 2016. p.475–9.

TABLES

Supplemental Table 1: Imaging parameters for 22 recent 2D RT-MRI publications that utilize state-of-the-art methodology, as selected by the authors of this review. Spatial and temporal resolutions are plotted in **Figure 2**.

App / Reference	Spatial Resolution (mm^2)	Temporal Resolution (ms/fps)	Notes
Cardiac			
Kowalik et al. 2012 (62)	3.5x3.5	20 ms (50 fps)	Flow to measure cardiac time intervals (1.5T) FOV: 500 x 500 mm Trajectory: Spiral PCMR Acceleration: x10 Reconstruction: Parallel imaging (UNFOLD-ed SENSE)
Bassett et al. 2013 (20)	2.0x2.0	47 ms (21 fps)	Ventricular volumes in Tachycardia (animal model. 3T) FOV: 260x260 mm Trajectory: Cartesian bSSFP Acceleration: x8 Reconstruction: Compressed sensing (*k-t* SPARSE-SENSE)
Kowallick et al. 2014 (98)	1.3x1.3	40 ms (25 fps)	Flow during Valsalva maneuver (3T) FOV: 192x192 mm Trajectory: Radial PCMR Acceleration: ~x20 Reconstruction: Non-linear inversion (NLINV)
Haji-Valizadeh et al. 2017 (90)	2.1x2.1	32 ms (31 fps)	Ventricular volumes in myocardial infarction (1.5T) and chronic kidney disease (3T) FOV: 300x300 mm Trajectory: Radial bSSFP Acceleration: x12 Reconstruction: Compressed sensing (GRASP)
Körperich et al. 2017 (96)	2.7x2.7	25 ms (40 fps)	Flow in Fontan Circulation (3T) FOV: 300x300 mm Trajectory: EPI PCMR Acceleration: x4 (plus Partial Fourier: 0.6)

			Reconstruction: Parallel imaging (SENSE)
Allen et al. 2018 (86)	2.0x2.0	42 ms (24 fps)	Ventricular volumes in Atrial Fibrillation (1.5T) FOV: 380x380 mm Trajectory: Cartesian bSSFP Acceleration: ~x10 Reconstruction: Compressed sensing (SPARSE-SENSE)
Steeden et al. 2018 (93)	1.7x1.7	30 ms (33 fps)	Ventricular volumes in children (1.5T) FOV: 350x350 mm Trajectory: Spiral bSSFP Acceleration: x12 Reconstruction: Compressed sensing (similar to GRASP)
Kowalik et al. 2019 (99)	1.8x1.8	27 ms (37 fps)	Flow in great vessels in children (1.5T) FOV: 450x450 mm Trajectory: Perturbed spiral PCMR Acceleration: x18 Reconstruction: Compressed sensing (similar to GRASP)
Interventional			
Unterberg-Buchwald et al. 2017 (133)	1.6x1.6	42 ms (24 fps)	Endomyocardial biopsies (animal model. 3T) FOV: 256x256 mm Trajectory: Radial bSSFP Acceleration: ~x6 Reconstruction: Non-linear inversion (NLINV) with 27ms reconstruction latency)
Rogers et al. 2017 (79)	2.2x3.3	78 – 250 ms (adjusted dynamically) (13 – 4 fps)	Diagnostic catheterization (1.5T) FOV: 400x400 mm Trajectory: Cartesian bSSFP Acceleration: x1 to x4 Reconstruction: Parallel imaging (GRAPPA)
Chubb et al. 2017 (122)	0.8x0.8	100 ms (10 fps)	Active catheterization for ablation (3D point localization of point-source microcoils. 1.5T) Sequence: Dedicated tracking sequence (modified fast-field echo)
Heidt et al. 2019 (131)	1.7x1.7	294 ms(plus 18 ms fat	Coronary catheterization with active guidewire (3T) FOV: 275x275 mm Trajectory: Radial bSSFP

		saturation per frame) (3 fps)	Acceleration: x1.5 Reconstruction: Gridding
Upper Airway			
Niebergall et al. 2013 (157)	1.5x1.5	33.3 ms (30 fps)	Speech task (3T) FOV: 192x192 mm Trajectory: Radial (FLASH) Acceleration: ~x13.3 Reconstruction: Non-linear inversion (NLINV)
Iltis et al. 2015 (158)	1.5x1.5	10 ms (100 fps)	Upper airway (fast tongue movements in elite horn players. 3T) FOV: 192x192 mm Trajectory: Radial (FLASH) Acceleration: ~x40 Reconstruction: Non-linear inversion (NLINV)
Lingala et al. 2016 (11)	2.4x2.4	12 ms (84 fps)	Speech task (vocal tract shaping. 1.5T) FOV: 200x200 mm Trajectory: Spiral (GRE) Acceleration: x6.5 Reconstruction: Compressed sensing (SPARSE-SENSE)
Olthoff et al.2016 (145)	1.3x1.3	40 ms (25 fps)	Swallowing task (3T) FOV: 192x192 mm Trajectory: Radial (FLASH) Acceleration: ~x10 Reconstruction: Non-linear inversion (NLINV)
Lingala et al. 2017 (54)	2.4x2.4	18 ms (56 fps)	Speech task (1.5T) FOV: 200x200 mm Trajectory: Spiral (GRE) Acceleration: x4.3 Reconstruction: Parallel imaging (Through-time GRAPPA)
Freitas et al. 2018 (155)	1.5x1.5	38 ms (26 fps)	Speech task to visualize velopharyngeal motion (3T) FOV: 190x190 mm Trajectory: Radial (FLASH) Acceleration: x2.5 Reconstruction: Total Generalized Variation

Ruthven et al. 2019 (55)	2.4x2.4	61 ms (16 fps)	Speech task (3T) FOV: 192x192 mm Trajectory: Radial (spoiled GRE) Acceleration: x5 Reconstruction: Parallel imaging (Through-time GRAPPA)
Musculoskeletal			
Fiorentino et al. 2013 (213)	1.6x1.6	331 ms (3 fps)	Rectus Femoris Knee Muscle movement (1.5T) FOV: 400x300 mm Trajectory: 2D Cartesian (spoiled GRE) Acceleration: x1 Reconstruction: Fourier transform
Krohn et al. 2016 (180)	0.75x0.75	67 ms (15 fps)	Temporomandibular joint movement (3T) FOV: 192x192 mm Trajectory: Radial (spoiled FLASH / refocused FLASH) Acceleration: ~x14 / ~x24 Reconstruction: Non-linear inversion (NLINV)
Henrichon et al. 2020 (178)	1.1x1.1	315 ms (3 fps)	Wrist movement (3T) FOV: 120x120 mm Trajectory: 2D Radial (FLASH) Acceleration: x1 Reconstruction: Gridding

FIGURE CAPTIONS

Figure 1: Publications involving RT-MRI. PubMed search: (("real-time MRI") OR ("real-time NMR") OR ("real-time magnetic resonance") OR ("real-time interactive MRI") OR ("RT-MRI")).

Figure 2: Scatterplot of 2D RT-MRI spatial and temporal resolution. Spatial resolution (x-axis) versus temporal resolution (y-axis) is plotted from 22 recent publications that utilize state-of-the-art methodology, as selected by the authors of this review, summarized in **Supplemental Table 1**. The gray shaded bar indicates the general spatio-temporal resolution tradeoff. All substantial deviations are due to variations in the field-of-view, use of parallel imaging, use of reconstruction constraints, and minimum acceptable signal-to-noise ratio.

Figure 3: Common sequences, sampling trajectories, and view orders used in 2D RT-MRI. **(A)** sequence diagrams of spoiled GRE and bSSFP, and the steady-state signal amplitude as a function of off-resonance Δf; Simulation parameters: TR=5 ms; flip angle = 5° for spoiled GRE; flip angle = 60° for bSSFP; myocardium T1/T2=950/50 ms; blood T1/T2=1500/250 ms (representative of 1.5T). **(B)** Non-Cartesian sampling trajectories of undersampled radial, single-shot spiral, and single-shot EPI. **(C)** View orders of multi-shot spiral of conventional 13-interleaf bit-reversed and golden-ratio, and unaliased FOV as a function of the number of interleaves [Reproduced from Ref (25)].

Figure 4: Illustration of cardiovascular RT-MRI. **(A)** Real-time cine imaging using tiny-golden angle radial bSSFP sequence at 1.5T, with 12x undersampling and compressive sensing reconstruction (TE/TR = 1.3/2.7 ms, flip angle = 70º, in-plane resolution = 2.1 mm, 32 ms temporal resolution, 31 fps). A movie can be found in **Supplemental Movie 1** [Adapted from Ref (90)]. **(B)** Real-time PCMR using perturbed spirals at 1.5T, with 18x undersampling and compressive sensing reconstruction. Top: Magnitude images, Bottom: Phase images (TE/TR = 1.9/6.7 ms, VENC = 200 cm/s, flip angle = 20º, in-plane resolution = 1.8 mm, 27 ms temporal resolution, 37 fps). A movie can be found in **Supplemental Movie 2** [Adapted from Ref (99)]. **(C)** Real-time imaging of the fetal heart (shown by arrow in first column) demonstrating gross fetal movement. Golden-angle radial bSSFP sequence at 1.5T, with 27x undersampling

and compressive sensing reconstruction (TR = 5.0 ms, flip angle = 70º, in-plane resolution = 1.0 mm, 74 ms temporal resolution, 14 fps). A movie can be found in **Supplemental Movie 3** [Adapted from Ref (109)].

Figure 5: Illustrations of RT-MRI for MRI-guided invasive procedures. Cardiovascular procedures are the most technically demanding for RT-MRI, and therefore are provided. **(A)** The position and orientation of catheter devices with two embedded microcoils are tracked on a previously acquired 3D volume for an electrophysiology procedure. Real-time device tracing is achieved using 3D gradient echo projection imaging (resolution 0.83mm, 10Hz tracking rate) [Reproduced from Ref (122)]. **(B)** Interactive RT-MRI used to navigate gadolinium filled balloon wedge end-hole catheter during diagnostic right heart catheterization (bSSFP, TE/TR = 1.44/2.88 ms, flip angle = 40º, in-plane resolution = 1.8 mm x 2.4 mm, GRAPPA rate 2, 200 ms temporal resolution, 5 fps) [Adapted from Ref (123)]. **(C)** Real-time MRI thermometry used to calculate thermal dose during therapeutic ablation procedure (Gradient echo EPI, TE/TR = 18-20/110 ms, flip angle = 60º, in-plane resolution = 1.6 mm x 1.6 mm, GRAPPA rate 2, 200 ms temporal resolution, 5 slices/s) [Adapted from Ref (134)].

Figure 6: Illustration of upper airway RT-MRI. **(A)** Speech production imaging using 13-interleave spiral GRE sequence at 1.5T (TE/TR = 0.8/6.0 ms, flip angle = 15º, in-plane resolution = 2.4 mm, 12 ms temporal resolution, 83 fps) [Adapted from Ref (214)]. **(B)** Sleep apnea study using simultaneous multi-slice radial GRE sequence at 3T (TE/TR = 3.7/6.5 ms, flip angle = 5º, slice thickness/gap = 7/3 mm, 3 slices, in-plane resolution = 1 mm, 96 ms temporal resolution, 10 fps) [Adapted from Ref (37)]. **(C)** Swallowing imaging of 10ml pineapple juice using radial FLASH sequence (TE/TR = 1.33/2.10ms, flip angle = 8º, in-plane resolution = 1.3 mm, 40 ms temporal resolution, 25 fps, 19 spokes) [Adapted from Ref (145)].

Figure 7: Illustration of three Musculoskeletal RT-MRI applications. **(A)** Knee RT-MRI highlighting flexion, extension, and the measurement of rectus femoris knee muscle moment arms [Adapted from Ref (213)]. **(B)** Wrist RT-MRI illustrating a radial-ulnar deviation maneuver, suitable for measuring dynamics of the scapholunate gap [Adapted from Ref

(177)]. **(C)** Temporomandibular joint RT-MRI illustrating the ability to track condyle movement during voluntary opening of the mouth [Adapted from Ref (180)].

Figure 8: Illustration of three ML/AI-based low-latency applications. **(A)** Image reconstruction of cardiovascular imaging; (left-to-right) the BH-bSSFP sequence and the RT radial sequence reconstructed with gridding, GRASP, and the residual U-Net. [Adapted from Ref (92)] **(B)** Spiral off-resonance deblurring of speech imaging; (left-to-right) GT, uncorrected, IR with GT field map, and the CNN. [Adapted from Ref (77)] **(C)** Needle detection and segmentation for ex vivo tissue RT-MRI; (left-to-right) Original image, needle detection and segmentation result using Mask R-CNN, result comparison against a reference. [Adapted from Ref (205)]. Note that "processing time" shown here is the time to run the neural networks and does not include the time to do the pre-processing of the data. (BH: breath-hold, GRASP: Golden-angle RAdial Sparse Parallel imaging, PT: processing time, GT: ground truth, IR: iterative reconstruction)

Figure 9: Demonstration of real-time bSSFP imaging using a high-performance low field (HPLF) MRI system (prototype 0.55T Aera, Siemens Healthcare, Erlangen, Germany). **(A)** Real-time bSSFP for MRI-guided invasive cardiovascular procedures (TE/TR = 2.0/4.0 ms, flip angle = 45º, in-plane resolution = 2mm, slice thickness = 8mm, GRAPPA rate 2, 250 ms temporal resolution, 4 fps). **(B)** Real-time bSSFP for dynamic intestinal imaging (TE/TR = 1.6/3.2ms, flip angle = 90º, in-plane resolution = 1.2mm, slice thickness = 10mm, GRAPPA rate 3, 1.2s temporal resolution for 6 slices, 0.8 fps). No bSSFP banding around the intestines is observed using the HPLF system configuration. **(C)** Real-time bSSFP for dynamic respiratory imaging (TE/TR = 1.21/2.4ms, flip angle = 70º, in-plane resolution = 1.8mm, slice-thickness = 15mm, GRAPPA rate 2, 250 ms temporal resolution, 4 fps). Due to the reduced susceptibility, higher quality imaging of lung parenchyma is feasible.

SUPPLEMENTAL MOVIE CAPTIONS

Supplemental Movie 1: Real-time cine imaging using tiny-golden angle radial bSSFP sequence at 1.5T, with 12x undersampling and compressive sensing reconstruction (TE/TR = 1.3/2.7ms, flip angle = 70º, in-plane resolution = 2.1 mm, 32 ms temporal resolution, 31 fps) [Reproduced from Ref (90)].

Supplemental Movie 2: Real-time PCMR using perturbed spirals at 1.5T, with 18x undersampling and compressive sensing reconstruction. Top: Magnitude images, Bottom: Phase images (TE/TR = 1.9/6.7 ms, VENC = 200 cm/s, flip angle = 20º, in-plane resolution = 1.8 mm, 27 ms temporal resolution, 37 fps) [Reproduced from Ref (99)].

Supplemental Movie 3: Real-time imaging of the fetal heart (shown by arrow in first column) demonstrating gross fetal movement. Golden-angle radial bSSFP sequence at 1.5T, with 27x undersampling and compressive sensing reconstruction (TR = 5.0 ms, flip angle = 70º, in-plane resolution = 1.0 mm, 74 ms temporal resolution, 14 fps) [Reproduced from Ref (109)].

Supplemental Movie 4: Real-time device tracing achieved using 3D fast-field echo projection imaging (spatial resolution 0.83mm, 100 ms temporal resolution, 10 fps). The position and orientation of catheter devices with two embedded microcoils are tracked on a previously acquired 3D volume for an electrophysiology procedure. [Reproduced from Ref (122)]

Supplemental Movie 5: Interactive real-time Cartesian bSSFP imaging used to guide a gadolinium-filled balloon wedge catheter during diagnostic right heart catheterization procedure. Interactive modification of slice planes, number of multiplanar image slices, saturation pulse, and acceleration are demonstrated. bSSFP, TE/TR = 1.44/2.88 ms, flip angle = 40º, in-plane resolution = 1.8 mm x 2.4 mm, GRAPPA rate 2, 200 ms temporal resolution, 5 fps. RV: Right Ventricle, MPA: Main pulmonary artery, RPA: right pulmonary artery. [Reproduced from Ref (123)]

Supplemental Movie 6: Real-time cardiac MR thermometry used for inline monitoring of heat dose during therapeutic radiofrequency ablation (70W for 40s), demonstrated in an animal model. Gradient echo EPI, TE/TR = 18-20/110 ms, flip angle = 60º, in-plane resolution = 1.6 mm x 1.6 mm, GRAPPA rate 2, 200 ms temporal resolution, 5 slices/s. [Adapted from Ref (134)]

Supplemental Movie 7: RT-MRI of speech production (fluent speech – rainbow passage) using 13-interleave spiral GRE sequence at 1.5T (TE/TR = 0.8/6ms, flip angle = 15º, in-plane resolution = 2.4 mm, 12 ms temporal resolution, 83 fps) [Reproduced from Ref (11)].

Supplemental Movie 8: RT-MRI of sleep apnea events using simultaneous multi-slice radial GRE sequence at 3T (TE/TR = 3.7/6.5 ms, flip angle = 5º, slice thickness/gap = 7/3 mm, 3 slices, in-plane resolution = 1 mm, 96 ms temporal resolution, 10 fps) [Reproduced from Ref (37)].

Supplemental Movie 9: RT-MRI of swallowing imaging of 10ml pineapple juice using radial FLASH sequence (TE/TR = 1.33/2.10ms, flip angle = 8º, in-plane resolution = 1.3 mm, 40 ms temporal resolution, 25 fps, 19 spokes) [Reproduced from Ref (145)].

Supplemental Movie 10: Knee RT-MRI highlighting flexion, extension, and the measurement of rectus femoris knee muscle moment arms [Reproduced from Ref (213)].

Supplemental Movie 11: Wrist RT-MRI illustrating a radial-ulnar deviation maneuver, suitable for measuring dynamics of the scapholunate gap [Reproduced from Ref (177)].

Supplemental Movie 12: Temporomandibular joint RT-MRI illustrating the ability to track condyle movement during voluntary opening of the mouth [Reproduced from Ref (180)].

Supplemental Movie 13: Illustration of ML/AI based low-latency Image reconstruction of cardiovascular imaging; Examples from two prospective patients; (left-to-right) the BH-bSSFP sequence and the RT radial sequence reconstructed with GRASP, the residual U-Net, and gridding. [Adapted from Ref (92)]

Supplemental Movie 14: Illustration of ML/AI based low-latency Spiral off-resonance deblurring of speech imaging; (left-to-right) GT, uncorrected, IR with GT field map, and the CNN. [Adapted from Ref (77)]

Supplemental Movie 15: Real-time bSSFP imaging using a high-performance low field (HPLF) MRI system (prototype 0.55T Aera, Siemens Healthcare, Erlangen, Germany). **(A)** Real-time bSSFP for MRI-guided invasive cardiovascular procedures (TE/TR = 2.0/4.0 ms, flip angle = 45º, in-plane resolution = 2 mm, slice thickness = 8 mm, GRAPPA rate 2, 250 ms temporal resolution, 4 fps). **(B)** Real-time bSSFP for dynamic intestinal imaging (TE/TR = 1.6/3.2ms, flip angle = 90º, in-plane resolution = 1.2 mm, slice thickness = 10 mm, GRAPPA rate 3, temporal resolution 1.2 s for 6 slices). **(C)** Real-time bSSFP for dynamic respiratory imaging (TE/TR = 1.21/2.4 ms, flip angle = 70, in-plane resolution = 1.8 mm, slice-thickness = 15 mm, GRAPPA rate 2, 250 ms temporal resolution, 4 fps). [(A) Based on Ref (210), (B) and (C) Unpublished Data]

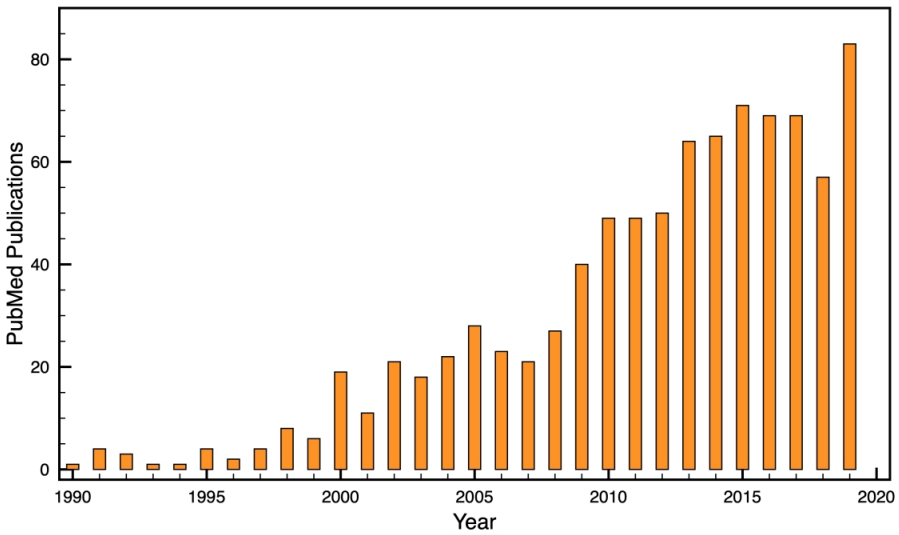

Figure 1: Publications involving RT-MRI. PubMed search: (("real-time MRI") OR ("real-time NMR") OR ("real-time magnetic resonance") OR ("real-time interactive MRI") OR ("RT-MRI")).

1071x636mm (72 x 72 DPI)

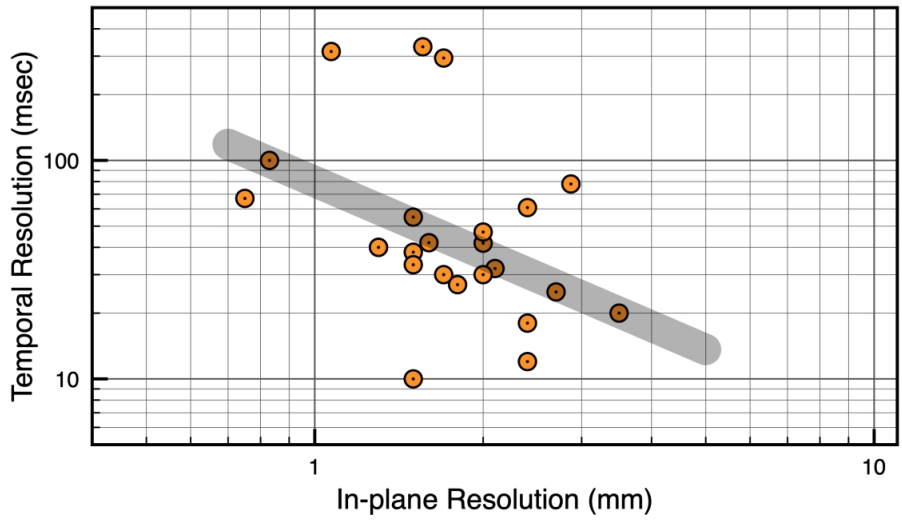

Figure 2: Scatterplot of 2D RT-MRI spatial and temporal resolution. Spatial resolution (x-axis) versus temporal resolution (y-axis) is plotted from 22 recent publications that utilize state-of-the-art methodology, as selected by the authors of this review, summarized in Supplemental Table 1. The gray shaded bar indicates the general spatio-temporal resolution tradeoff. All substantial deviations are due to variations in the field-of-view, use of parallel imaging, use of reconstruction constraints, and minimum acceptable signal-to-noise ratio.

822x478mm (72 x 72 DPI)

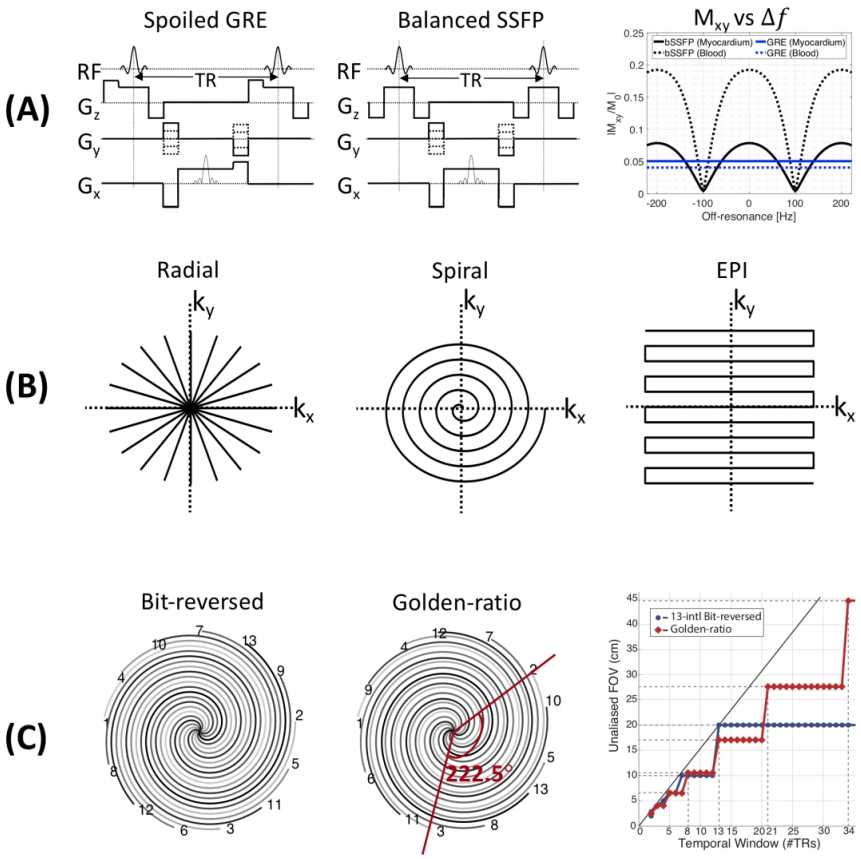

Figure 3: Common sequences, sampling trajectories, and view orders used in 2D RT-MRI. (A) sequence diagrams of spoiled GRE and bSSFP, and the steady-state signal amplitude as a function of off-resonance Δf; Simulation parameters: TR=5ms; flip angle = 5° for spoiled GRE; flip angle = 60° for bSSFP; myocardium T1/T2=950/50ms; blood T1/T2=1500/250ms (representative of 1.5T). (B) Non-Cartesian sampling trajectories of undersampled radial, single-shot spiral, and single-shot EPI. (C) View orders of multi-shot spiral of conventional 13-interleaf bit-reversed and golden-ratio, and unaliased FOV as a function of the number of interleaves [Reproduced from Ref (25)].

179x177mm (300 x 300 DPI)

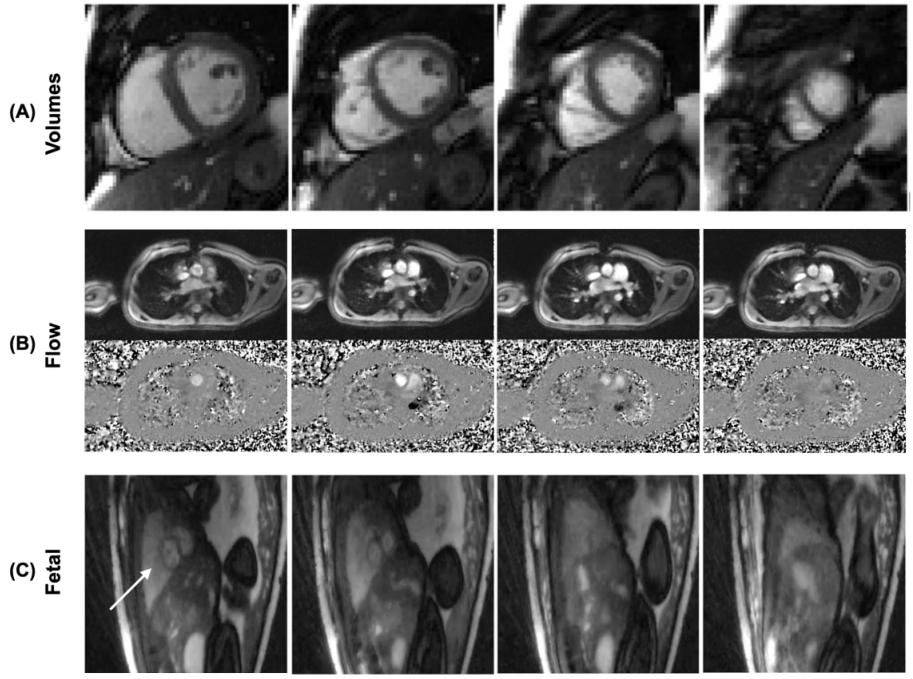

Figure 4: Illustration of cardiovascular RT-MRI. (A) Real-time cine imaging using tiny-golden angle radial bSSFP sequence at 1.5T, with 12x undersampling and compressive sensing reconstruction (TE/TR = 1.3/2.7 ms, flip angle = 70º, in-plane resolution = 2.1 mm, 32 ms temporal resolution, 31 fps). A movie can be found in Supplemental Movie 1 [Adapted from Ref (90)]. (B) Real-time PCMR using perturbed spirals at 1.5T, with 18x undersampling and compressive sensing reconstruction. Top: Magnitude images, Bottom: Phase images (TE/TR = 1.9/6.7 ms, VENC = 200 cm/s, flip angle = 20º, in-plane resolution = 1.8 mm, 27 ms temporal resolution, 37 fps). A movie can be found in Supplemental Movie 2 [Adapted from Ref (99)]. (C) Real-time imaging of the fetal heart (shown by arrow in first column) demonstrating gross fetal movement. Golden-angle radial bSSFP sequence at 1.5T, with 27x undersampling and compressive sensing reconstruction (TR = 5.0 ms, flip angle = 70º, in-plane resolution = 1.0 mm, 74 ms temporal resolution, 14 fps). A movie can be found in Supplemental Movie 3 [Adapted from Ref (109)].

149x111mm (600 x 600 DPI)

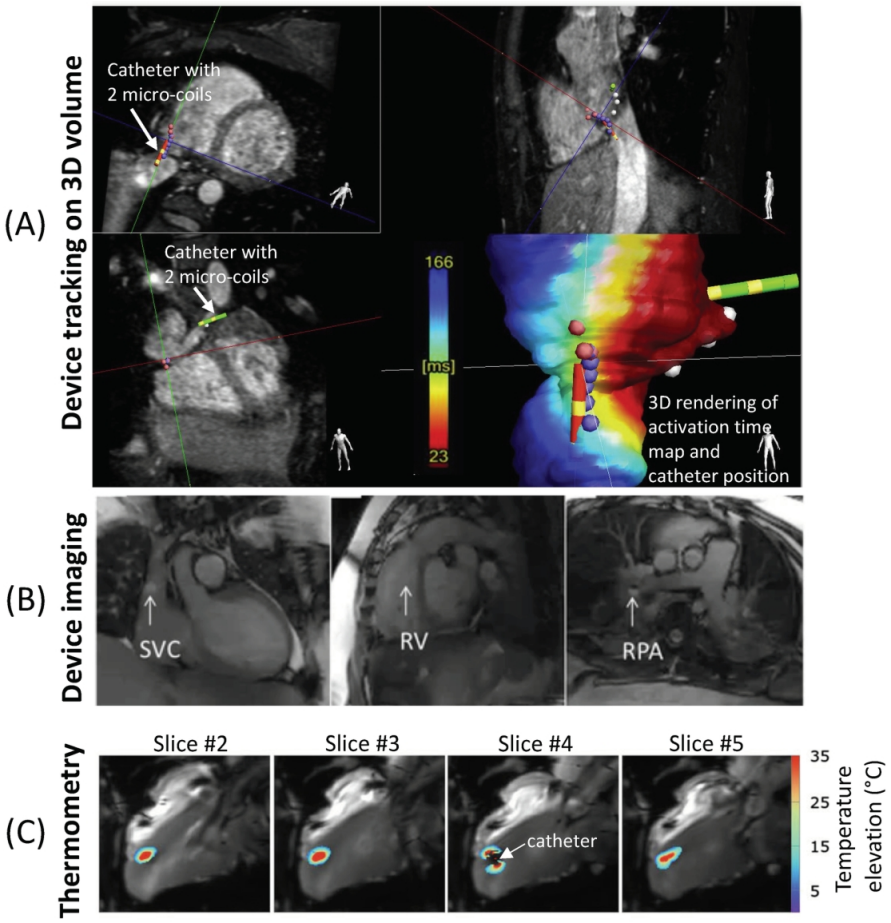

Figure 5: Illustrations of RT-MRI for MRI-guided invasive procedures. Cardiovascular procedures are the most technically demanding for RT-MRI, and therefore are provided. (A) The position and orientation of catheter devices with two embedded microcoils are tracked on a previously acquired 3D volume for an electrophysiology procedure. Real-time device tracing is achieved using 3D gradient echo projection imaging (resolution 0.83mm, 10Hz tracking rate) [Reproduced from Ref (122)]. (B) Interactive RT-MRI used to navigate gadolinium filled balloon wedge end-hole catheter during diagnostic right heart catheterization (bSSFP, TE/TR = 1.44/2.88 ms, flip angle = 40º, in-plane resolution = 1.8 mm x 2.4 mm, GRAPPA rate 2, 200 ms temporal resolution, 5 fps) [Adapted from Ref (123)]. (C) Real-time MRI thermometry used to calculate thermal dose during therapeutic ablation procedure (Gradient echo EPI, TE/TR = 18-20/110 ms, flip angle = 60º, in-plane resolution = 1.6 mm x 1.6 mm, GRAPPA rate 2, 200 ms temporal resolution, 5 slices/s) [Adapted from Ref (134)].

158x161mm (300 x 300 DPI)

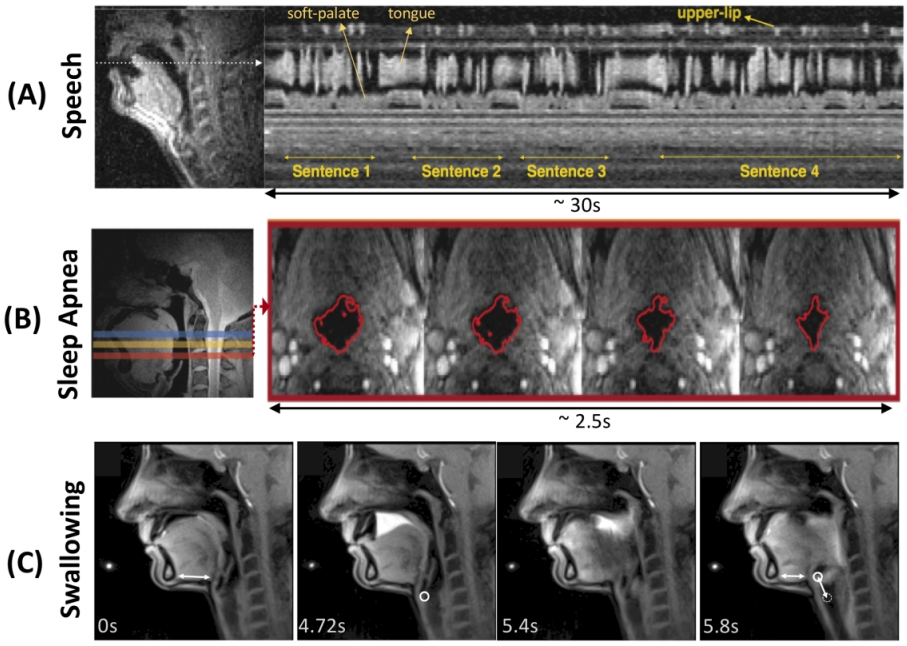

Figure 6: Illustration of upper airway RT-MRI. (A) Speech production imaging using 13-interleave spiral GRE sequence at 1.5T (TE/TR = 0.8/6.0 ms, flip angle = 15º, in-plane resolution = 2.4 mm, 12 ms temporal resolution, 83 fps) [Adapted from Ref (214)]. (B) Sleep apnea study using simultaneous multi-slice radial GRE sequence at 3T (TE/TR = 3.7/6.5 ms, flip angle = 5º, slice thickness/gap = 7/3 mm, 3 slices, in-plane resolution = 1 mm, 96 ms temporal resolution, 10 fps) [Adapted from Ref (37)]. (C) Swallowing imaging of 10ml pineapple juice using radial FLASH sequence (TE/TR = 1.33/2.10ms, flip angle = 8º, in-plane resolution = 1.3 mm, 40 ms temporal resolution, 25 fps, 19 spokes) [Adapted from Ref (145)].

208x156mm (300 x 300 DPI)

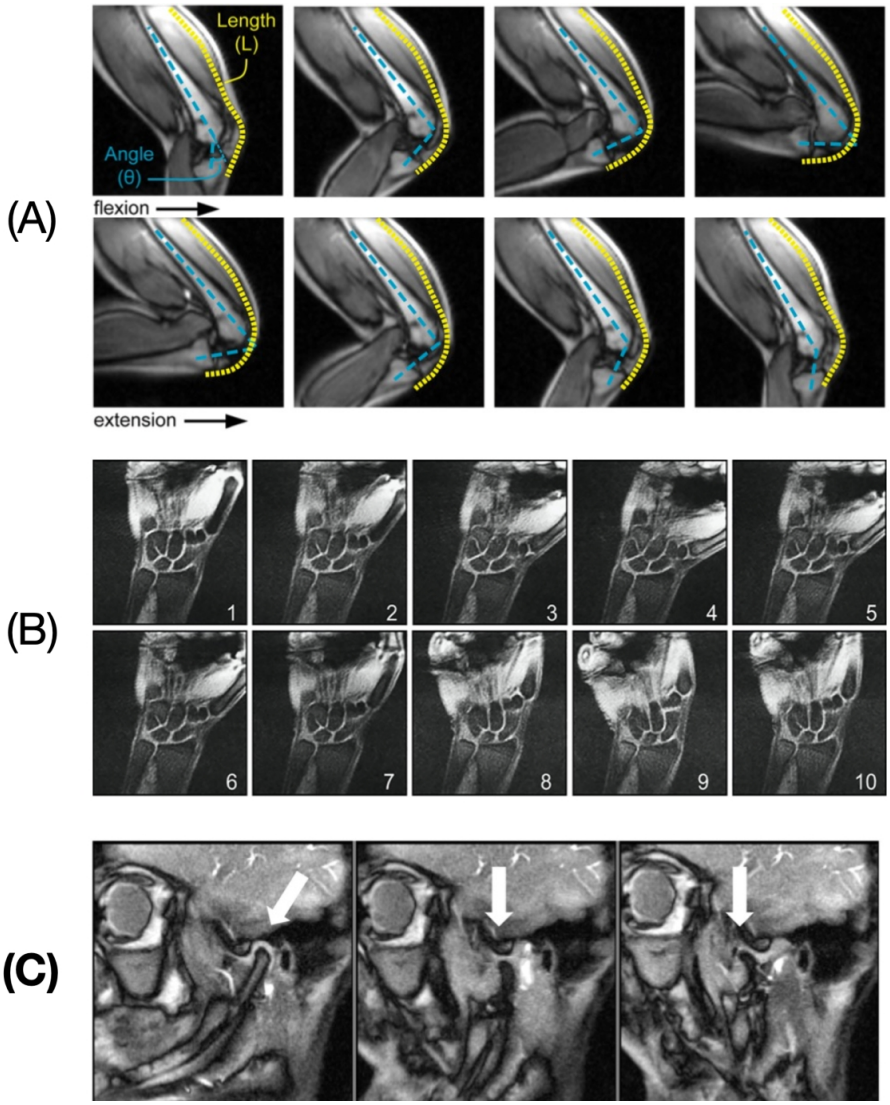

Figure 7: Illustration of three Musculoskeletal RT-MRI applications. (A) Knee RT-MRI highlighting flexion, extension, and the measurement of rectus femoris knee muscle moment arms [Adapted from Ref (213)]. (B) Wrist RT-MRI illustrating a radial-ulnar deviation maneuver, suitable for measuring dynamics of the scapholunate gap [Adapted from Ref (177)]. (C) Temporomandibular joint RT-MRI illustrating the ability to track condyle movement during voluntary opening of the mouth [Adapted from Ref (180)].

166x202mm (300 x 300 DPI)

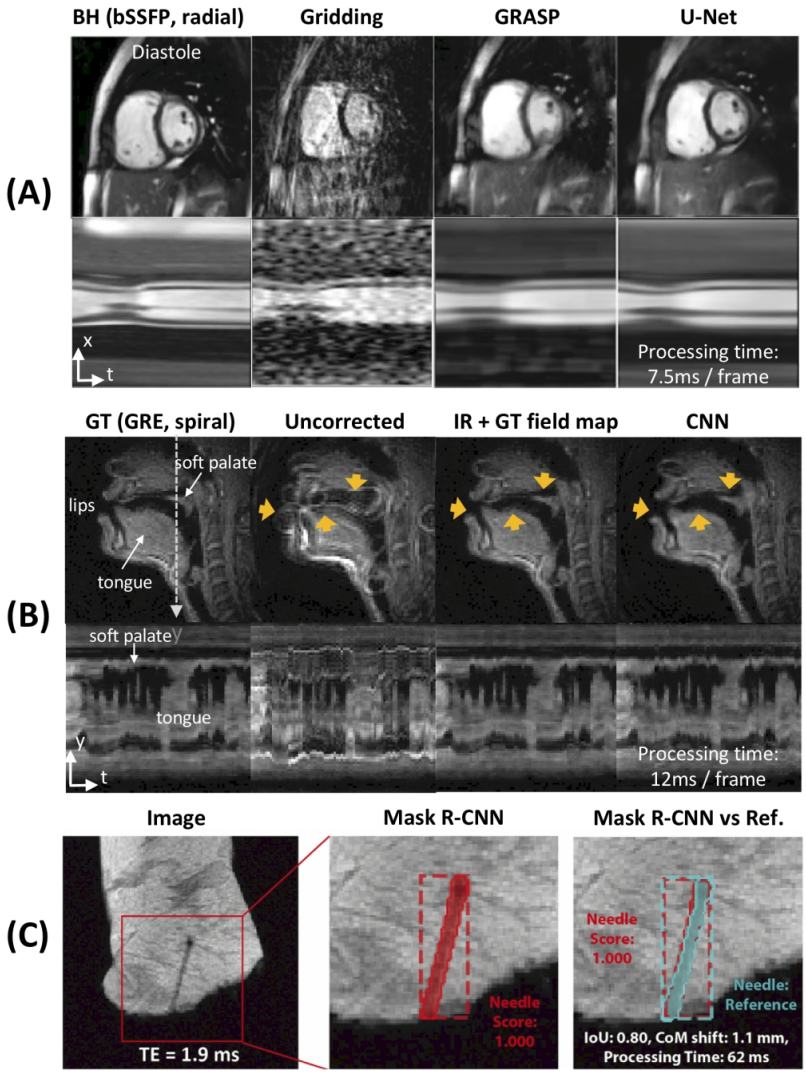

Figure 8: Illustration of three ML/AI-based low-latency applications. (A) Image reconstruction of cardiovascular imaging; (left-to-right) the BH-bSSFP sequence and the RT radial sequence reconstructed with gridding, GRASP, and the residual U-Net. [Adapted from Ref (92)] (B) Spiral off-resonance deblurring of speech imaging; (left-to-right) GT, uncorrected, IR with GT field map, and the CNN. [Adapted from Ref (77)] (C) Needle detection and segmentation for ex vivo tissue RT-MRI; (left-to-right) Original image, needle detection and segmentation result using Mask R-CNN, result comparison against a reference. [Adapted from Ref (205)]. Note that "processing time" shown here is the time to run the neural networks and does not include the time to do the pre-processing of the data. (BH: breath-hold, GRASP: Golden-angle RAdial Sparse Parallel imaging, PT: processing time, GT: ground truth, IR: iterative reconstruction)

160x215mm (300 x 300 DPI)

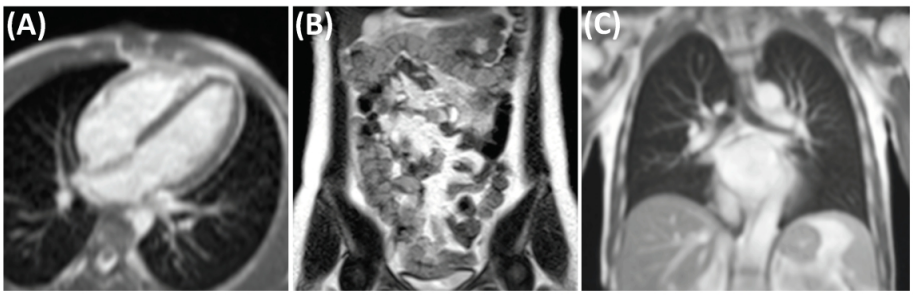

Figure 9: Demonstration of real-time bSSFP imaging using a high-performance low field (HPLF) MRI system (prototype 0.55T Aera, Siemens Healthcare, Erlangen, Germany). (A) Real-time bSSFP for MRI-guided invasive cardiovascular procedures (TE/TR = 2.0/4.0 ms, flip angle = 45º, in-plane resolution = 2mm, slice thickness = 8mm, GRAPPA rate 2, 250 ms temporal resolution, 4 fps). (B) Real-time bSSFP for dynamic intestinal imaging (TE/TR = 1.6/3.2ms, flip angle = 90º, in-plane resolution = 1.2mm, slice thickness = 10mm, GRAPPA rate 3, 1.2s temporal resolution for 6 slices, 0.8 fps). No bSSFP banding around the intestines is observed using the HPLF system configuration. (C) Real-time bSSFP for dynamic respiratory imaging (TE/TR = 1.21/2.4ms, flip angle = 70º, in-plane resolution = 1.8mm, slice-thickness = 15mm, GRAPPA rate 2, 250 ms temporal resolution, 4 fps). Due to the reduced susceptibility, higher quality imaging of lung parenchyma is feasible.

338x108mm (247 x 247 DPI)